Nanosized ammonia borane for solid-state hydrogen storage: Outcomes, limitations, challenges and opportunities

Kevin Turani-I-Belloto, Carlos Castilla-Martinez, Didier Cot, Eddy Petit, Sofian Benarib, Umit Demirci

Nanosized ammonia borane for solid-state hydrogen storage: Outcomes, limitations, challenges and opportunities

Kevin TURANI-I-BELLOTO, Carlos A. CASTILLA-MARTINEZ, Didier COT, Eddy PETIT, Sofian BENARIB, Umit B. DEMIRCI *

Institut Européen des Membranes, IEM – UMR 5635, ENSCM, CNRS, Univ Montpellier, Montpellier, France

* *Corresponding author*: umit.demirci@umontpellier.fr

Abstract

Ammonia borane NH_3BH_3 (AB), a material for solid-state hydrogen storage, can be nanosized by confinement into the porosity of a scaffold like mesoporous silica, carbon cryogel, graphene oxide, ZIF-8 as a metal organic framework, poly(methyl acrylate), boron nitride and manganese oxide. In doing so, nanosized AB is destabilized and shows better dehydrogenation properties than bulk AB in terms of temperature, activation energy, enthalpy and kinetics. Such improvements are due to the confinement-driven nanosizing effect, but not only. A catalytic effect may also have a contribution and, in some cases, it even overpasses the nanosizing effect. These effects are explained in detail herein. The present review aims at reporting the outcomes of the AB confinement strategy to help understand the advantages and to identify the limitations which are still not adequately defined. Based on this analysis, the challenges ahead are listed and discussed, and it appears that there are new opportunities to explore. Though nanosized AB is not mature enough for implementation, it has the potential to be developed further. Avenues worth exploring are given.

Keywords

Ammonia borane; Confinement; Hydrogen storage; Nanoconfinement; Nanosizing.

Abbreviations

B-N(-H) compounds

AB	**A**mmonia **B**orane NH_3BH_3
ADB	**A**mino**D**i**B**orane $NH_2B_2H_5$
BN	**B**oron **N**itride
BNM	**B**oron **N**itride **M**onolith
BNNP	**B**oron **N**itride **N**ano**P**olyhedra
BZ	**B**ora**Z**ine $B_3N_3H_6$
DADB	**D**i**A**mmoniate of **D**i**B**orane $[(NH_3)_2BH_2]^+[BH_4]^-$
DB	**D**i**B**orane B_2H_6
hBN	**h**exagonal **B**oron **N**itride
PB	**P**oly**B**orazylene $BNH_{<2}$
PAB	**P**oly**A**mino**B**orane $[NH_2BH_2]_n$
PIB	**P**oly**I**mino**B**orane $[NHBH]_n$

Carbonaceous scaffolds

AC	**A**ctivated **C**arbon
BNCC	**B**oron- and **N**itrogen-modified **C**arbon **C**ryogel
CC	**C**arbon **C**ryogel
CCC	**C**oherent **C**arbon **C**ryogel
CMK-3	**C**arbon **M**esostructured from **K**orea No. **3**
CMK-5	**C**arbon **M**esostructured from **K**orea No. **3**
GO	**G**raphene **O**xide
MC	**M**icroporous **C**arbon
PAF-1	**P**orous **A**romatic **F**ramework No. **1**

Manganese oxide

MOHC	**M**anganese **O**xide **H**ollow **C**ube
MOHS	**M**anganese **O**xide **H**ollow **S**phere

Metal organic frameworks and few of the related organic linkers

BDC	1,4-**B**enzene**D**i**C**arboxylate
BTC	1,3,5-**B**enzene**T**ri**C**arboxylate
IRMOF	**I**so**R**eticular **M**etal **O**rganic **F**ramework
JUC	**J**ilin **U**niversity **C**hina
MIL	**M**aterials of the "**I**nstitut **L**avoisier"
MOF	**M**etal **O**rganic **F**ramework

UiO	**U**niversitetet **i** **O**slo
ZIF	**Z**eolitic **I**midazolate **F**ramework

Miscellaneous

GHSC	**G**ravimetric **H**ydrogen **S**torage **C**apacity
TRL	**T**echnological **R**eadiness **L**evel
VHSC	**V**olumetric **H**ydrogen **S**torage **C**apacity

Organic polymers

PAM	**P**oly**A**crila**M**ide
PEO	**P**oly**E**thylene **O**xide
PMA	**P**oly(**M**ethyl **A**crylate)
PMMA	**P**oly(**M**ethyl **M**eth**A**crylate)
PS	**P**oly**S**tyrene
PSDB	**P**oly(**S**tyrene-co-**D**ivinyl**B**enzene)
PVP	**P**oly**V**inyl**P**yrrolidone

Silica

MCF	**M**esoporous **C**ellular **F**oam
MCM-41	**M**obil **C**omposition of **M**atter No. **41**
SBA-15	**S**anta **B**arbara **A**morphous**-15**
SHNS	**S**ilica **H**ollow **N**ano**S**pheres

Techniques

DSC	**D**ifferential **S**canning **C**alorimetry
FTIR	**F**ourier **T**ransform **I**nfra**R**ed
MAS NMR	**M**agic-**A**ngle **S**pinning **N**uclear **M**agnetic **R**esonance
PDF	**P**air **D**istribution **F**unction
UV-Vis	**U**ltra**V**iolet**-Vis**ible
XRD	**X**-**R**ay **D**iffraction
XPS	**X**-ray **P**hotoelectron **S**pectroscopy

1. Introduction

Molecular hydrogen H_2 is a very promising energy carrier because it has a high gravimetric energy density with 120-142 MJ kg^{-1}, and its oxidation (or combustion) is straightforward resulting in the formation of water only:

$$H_2\ (g) + ½\ O_2\ (g) \rightarrow H_2O\ (g) \quad (1)$$

This is an attractive feature. This makes H_2 position itself as a key alternative to fossil fuels (e.g. methane CH_4) that generate carbon dioxide CO_2 (together with H_2O) on combustion. The big picture is much more complex, that is why, the deployment of the so-called hydrogen economy has been until recently slow [1,2]. For example, there are still technical and technological challenges touching, among others, production [3] and storage [4].

Storage of H_2, the lightest gas, is particularly problematic. A first approach, called physical storage, is to compress (200-800 bar) or to liquefy (−253 °C) H_2. Compression is the most mature technology [5]. A second approach is to focus on materials [6,7]. Sorbents (porous scaffolds) have allowed cryo-adsorbing H_2 (i.e. physisorption) at temperatures (e.g. −196 °C) higher than the aforementioned temperature [8]. Hydrides (metallic, complex, and chemical) have been developed. They are made of elements like magnesium, aluminum and boron that chemically bind atomic hydrogen [9,10]. This is solid-state hydrogen storage (also called chemical hydrogen storage).

As solid-state hydrogen storage materials, B-N-H compounds have shown attractive features, especially high gravimetric and volumetric hydrogen densities [11]. A typical representative is ammonia borane NH_3BH_3 (AB). Long sought by Schlesinger and co-workers [12] but discovered by Shore and Parry in the mid-1950s [13], AB was re-discovered in the mid-2000s as a promising hydrogen storage material. AB has a gravimetric H density of 19.5 wt. %, making it one of the most hydrogen dense molecules. It is stable at ambient conditions and under inert atmosphere. Put in water, and in the presence of a catalyst, it hydrolyzes generating H_2 [14]:

$$NH_3BH_3\ (aq) + 4\ H_2O\ (l) \rightarrow NH_4^+\ (aq) + B(OH)_4^-\ (aq) + 3\ H_2\ (g) \quad (2)$$

Presented as an alternative to the hydrolysis of sodium borohydride $NaBH_4$, the hydrolysis of AB has been widely investigated while almost exclusively focusing on the development of active and efficient metal-based catalysts [15].

Another appealing property of AB is that it carries two types of H atoms, three protic hydrogens $H^{\delta+}$ through the NH_3 moiety and three hydridic hydrogens $H^{\delta-}$ by the BH_3 group, and all of these hydrogens are involved in dihydrogen $H^{\delta+}\cdots H^{\delta-}$ interactions [16]. Under heating, they react together and form H_2. In fact, bulk AB decomposes rather than it dehydrogenates: it melts at about 100 °C and concomitantly decomposes through a two-step process over the temperature range 100-200 °C (Figure 1). Gaseous products mainly consisting of H_2 and borazine $B_3N_3H_6$ (BZ) are produced [17], and a solid polymeric residue of complex composition forms [18]. Heated at isothermal conditions, i.e. at a constant temperature below the melting point like 88 °C, bulk AB dehydrogenates via the formation of diammoniate of diborane $[(NH_3)_2BH_2]^+[BH_4]^-$ (DADB) and through a mechanistic pathway implying three successive steps of induction, nucleation and growth [19]; accordingly, AB releases one equivalent of H_2 (Figure 2). In reality, the overall decomposition process is more complex. First, aside from the aforementioned dihydrogen $H^{\delta+}\cdots H^{\delta-}$ interactions, homopolar $H^{\delta-}\cdots H^{\delta-}$ and $H^{\delta+}\cdots H^{\delta+}$ interactions have significant contribution in the release of H_2 [20-23]. This leads to B–B and N–N coupling reactions and thus to polymeric residues with B–B and N–N bonds in addition to the expected B–N bonds. Second, with bulk AB, the process is heterogeneous [24]. All of the AB molecules do not decompose simultaneously, conducing to a mixture of AB, DADB and various polymeric species. In conclusion, AB as a bulk material is not suitable for solid-state hydrogen storage. Efforts have then focused on finding strategies to destabilize AB in order to make it release pure H_2 at temperatures below 100 °C. With the discovery of an effective re-hydrogenation process [25] that was applied to polyborazylene (PB) (Figure 3), another goal has been to dehydrogenate AB to form PB as single solid residue in a selective way.

To date, five major destabilization strategies have been developed, such as: solubilization of AB in an anhydrous organic solvent like tetrahydrofuran and in the presence of a metal-based homogenous catalyst [26] like iridium pincer complex [27], palladium pincer complex [28] and N-heterocyclic carbene nickel [29]; addition of an excess of AB into an ionic liquid like 1-butyl-3-methylimidazolium chloride [30]; addition of a solid-state dopant like hexachloroplatinic acid H_2PtCl_6 [31] or ammonium chloride NH_4Cl [32] to solid-state AB; nanosizing AB by confining it into the porosity of a porous material (also called scaffold or host material) like mesoporous silica SBA-15 [33]; and, chemical modification of AB by

substitution of one $H^{\delta+}$ of the NH_3 moiety by a metal cation to obtain amidoborane derivatives like lithium amidoborane $LiNH_2BH_3$ [34].

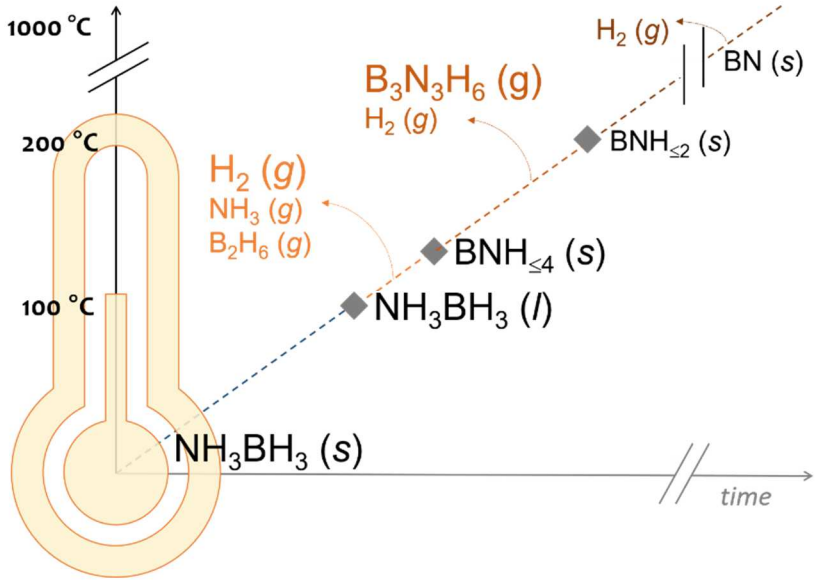

Figure 1. Schematic representation of the thermolytic decomposition of AB under heating at constant heating rate, from 0 to 1000 °C.

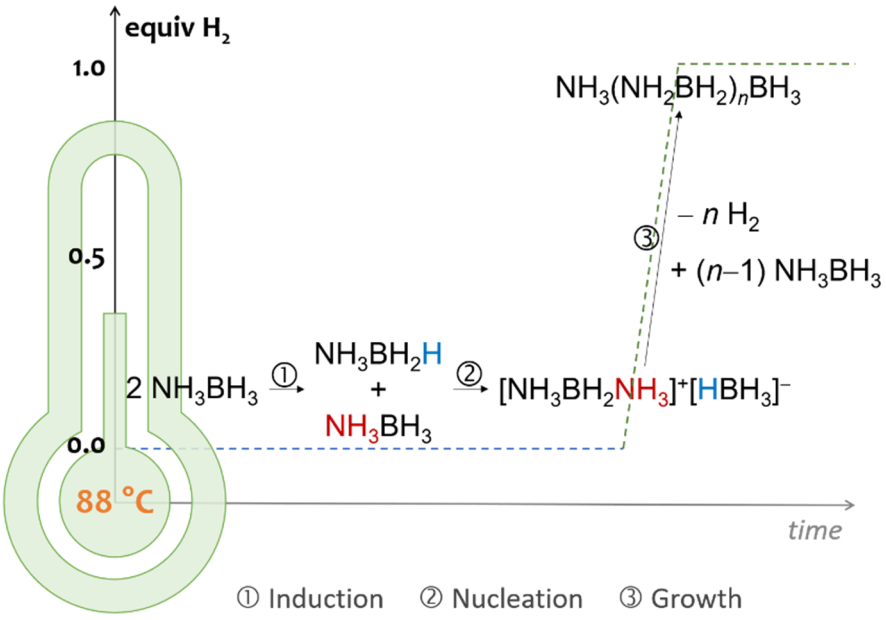

Figure 2. Dehydrogenation of bulk AB via the formation of DADB $[(NH_3)_2BH_2]^+[BH_4]^-$ and through a mechanistic pathway implying three successive steps of induction, nucleation and growth

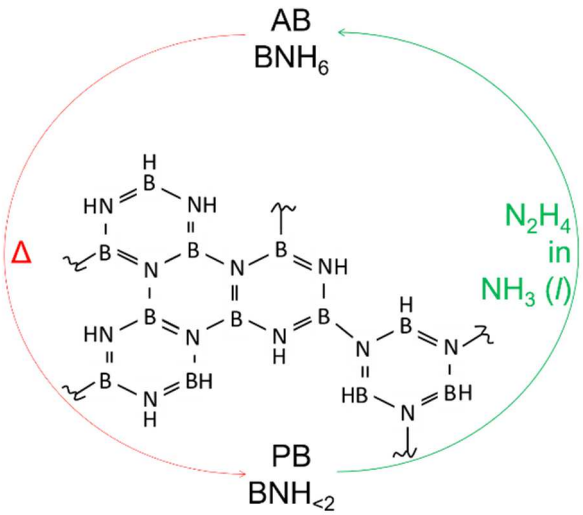

Figure 3. Hydrogen cycle with AB and PB ($BNH_{<2}$): dehydrogenation of AB under heating resulting in PB, and chemical recycling of PB into AB in the presence of N_2H_4 in liquid NH_3.

The confinement strategy is particularly appealing [35-38]. There are several reasons for claiming this. A priori, the used scaffold is inert towards AB. Infiltrated and confined AB is in the form of nanoparticles, having improved thermodynamics and kinetics of decomposition while dehydrogenation is favored. Solvents like ionic liquids, with high boiling points and that are difficult to evaporate, are not used. Unanchored catalysts or doping agents that may be difficult to separate from dehydrogenated AB are not used. No other element than B, N, and H is involved, unlike for amidoboranes. Since the seminal study using mesoporous silica SBA-15 [33], a number of scaffolds, of different natures, have been investigated for nanosizing AB by confinement [39]. All improve the dehydrogenation properties of AB. However, all are not so inert towards AB. In fact, the role of the scaffold has proven that it is more complicated than that which is mentioned above.

The present review scans 15 years of research dedicated to the AB confinement in order to bring the most important achievements out, highlight the role (or the roles) of the scaffolds used so far, discuss the main challenges ahead, and put the strategy aiming at nanosizing AB in perspective. The next section focuses firstly on silica as it was the first scaffold reported in the field. Then follows the other scaffolds: carbonaceous materials, metal organic frameworks (MOFs), polymers, boron nitride structures and manganese oxide hollow particles. Hereafter AB confined into the porosity of a scaffold is denoted AB@scaffold and is also called composite.

2. The scaffolds reported so far

The AB@scaffold composites presented herein all have better dehydrogenation properties than bulk AB. This applies in terms of e.g. onset temperature of dehydrogenation, enthalpy of dehydrogenation, and apparent activation energy. For bulk AB, the values generally reported are comparable to 100 °C, –21 kJ mol^{-1}, and ≥160 kJ mol^{-1}, respectively. Though some examples of values and performance are given hereafter for illustration, it does not appear opportune and relevant to propose an extensive comparison of the aforementioned temperature and energies. The rationale behind this is that there are discrepancies in the experimental conditions, making any comparison risky; indeed, scaffolds with different surface properties were used, the AB@scaffold preparation conditions were different, and the dehydrogenation experiments were performed in different experimental conditions and using different methods and/or apparatuses. For example, the decomposition behavior of bulk AB was reported to be different for a series of AB samples synthesized through different pathways as well as for a same sample but analyzed with different analyzers [40,41]. Hence, the following sections essentially focus on the factors behind the improvements.

2.1. Silica

Gutowska et al. [33] demonstrated that a saturated methanolic solution of AB could be infiltrated by capillary action into the mesoporosity of silica SBA-15, precisely into nanochannels of 7.5 nm in diameter parallelly and hexagonally aligned (Figure 4). In doing so, AB@SBA-15 was produced. The specific surface area of AB@SBA-15 was measured as <50 m^2 g^{-1} (versus 900 m^2 g^{-1} before infiltration) and the amount of infiltrated AB was determined as 50 wt. %. These two features indicated a successful confinement of AB into the scaffold. Elsewhere, the infiltration of AB was successfully performed by using tetrahydrofuran instead of methanol. For instance, Zhang et al. [42] worked with porous silica hollow nanospheres (SHNS; pore diameter of about 200 nm, specific surface area of 263 m^2 g^{-1}, and total pore volume of 0.56 m^3 g^{-1}) as scaffolds, and after infiltration of AB using tetrahydrofuran as a solvent, AB@SHNS had modified textural properties, with a specific surface area of <15 m^2 g^{-1} and a total pore volume of <0.2 m^3 g^{-1}. Sullivan et al. [43] also used tetrahydrofuran as a solvent of AB while aiming at comparing three mesoporous silicas, i.e. MCM-41 (668 m^2 g^{-1} and pore size of 3.4 nm), SBA-15 (497 m^2 g^{-1} and pore size of 4.3

nm), and MCF (217 m^2 g^{-1} and pore size of 18 nm). The best destabilization effect was obtained with MCF, namely the scaffold having the bigger pores and the lower specific surface area, followed by SBA-15 and MCM-41. This was explained by the role played by the solvent: AB dissolved in tetrahydrofuran forms extended linked (polymeric) species that cannot effectively diffuse inside the small pores of e.g. MCM-41.

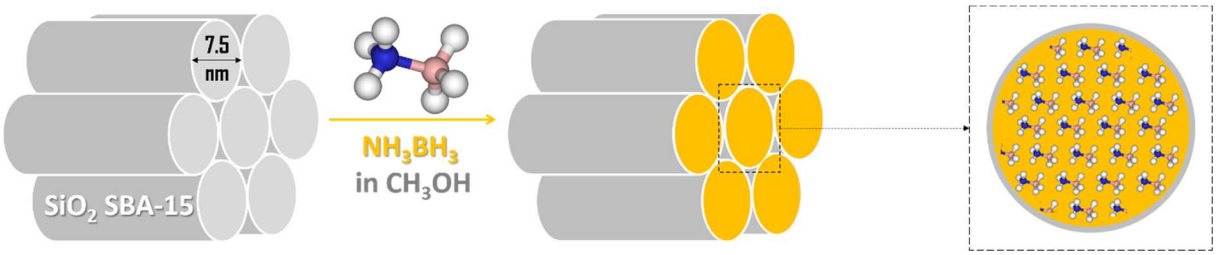

Figure 4. Schematic representation of the infiltration into the hexagonally arranged nanochannels of mesoporous silica SBA-15 while using a methanolic solution of ammonia borane NH_3BH_3.

Whatever the solvent used or the infiltration approach considered, AB must be completely confined. AB that is not confined, also called excess of AB, forms aggregates outside the scaffold porosity and, under heating, it is very similar to bulk AB. Wang et al. [44] showed that when the loading of AB exceeded the 50 wt. %, AB made aggregates outside the meso-channels of MCM-41. For loadings of ≤50 wt. %, AB uniformly coated on meso-channels.

All of the AB@scaffold composites showed improved thermolytic dehydrogenation properties in comparison with bulk AB. For example, the seminal AB@SBA-15, when heated at 1 °C min^{-1}, started to dehydrogenate from 50 °C [33]. In another study where SBA-15 and MCM-41 were used, comparable onset temperatures of dehydrogenation were measured [45]. A lower onset temperature of dehydrogenation (38 °C) was seen for AB (60 wt. %) confined into the porosity of a silica aerogel (887 m^2 g^{-1} and 1.94 cm^3 g^{-1}) [46]. Confined AB has modified thermodynamic properties. With AB@SBA-15, the enthalpy of H_2 loss was almost neutral, namely of −1 kJ mol^{-1} [33]. An enthalpy of −11 kJ mol^{-1} was measured for AB confined into silica aerogel, which had some AB outside the porosity behaving then as bulk AB [46]. The value −11 kJ mol^{-1} would be an average value between −21 kJ mol^{-1} for bulk AB and e.g. −1 kJ mol^{-1} for confined AB. With AB@SBA-15, the apparent activation energy of dehydrogenation was calculated as being 67 kJ mol^{-1} [33]. For AB@SNHS, the apparent activation energy was found to be 97.6 kJ mol^{-1} [42]. An energy of 104-109 kJ mol^{-1} was

calculated for AB confined into the porosity of silica MCM-41 nanospheres (diameter of 200 nm, and specific surface area of 726 m^2 g^{-1}) [47].

The purity of the released H_2 is controversial. On the one hand, released H_2 was found to be pure [48,49]. On the other hand, gaseous by-products were detected. Gutowska et al. [33] noticed, for AB@SBA-15, that the amount of released BZ was mitigated, but not avoided. Similar observation was reported by Lai et al. [45] for AB confined into SBA-15 or MCM-41. Further mitigation of BZ was achieved by doping the scaffold with Pd, Ni or Pt nanoparticles [50]. Some diborane B_2H_6 (DB), notably at around 100°C, and significant amounts of NH_3 were also detected. Worst of all, the amount of NH_3 was found to be greater than for bulk AB. This was explained by the breaking of the B–N bond of AB driven by O of surface Si–O–Si and SiO–H (Figure 5ab). For AB confined into three different mesoporous silicas (SBA-15, MCM-41 and MCF), Sullivan et al. [43] did not detect, in the gas stream, BZ nor any other volatile product. Instead they detected gaseous AB. It was suggested that BZ may decompose when in contact with the surface of silica to form the observed gaseous AB. Focusing more in detail on AB@MCF, Sullivan et al. concluded that the surface SiO–H groups play a more important role than the surface Si–O–Si in disrupting the AB lattice through interactions between SiO–H and NH_3 of AB (Figure 5c).

The better dehydrogenation properties of AB@scaffold can be explained by different positive effects. The first one is related to nanosizing, in other words, to the reduction of the AB particles size [47,48]. The as-formed AB nanoparticles have more defect sites initiating dehydropolymerization at lower temperatures [33]. Furthermore, the diffusion distances are reduced, facilitating the formation and release of H_2 [51].

The second positive effect has been attributed to the role of $H^{\delta+}$ of the SiO–H groups. This effect is generally discussed in terms of catalytic activation [52]. Zhang et al. [42], by using vibrational spectroscopy techniques and doing density functional theory calculations, showed that dihydrogen O–$H^{\delta+}\cdots H^{\delta-}$–B interactions between the surface SiO–H groups and the BH_3 groups of AB exist, and that they are stronger than the dihydrogen $H^{\delta+}\cdots H^{\delta-}$ interactions between the AB molecules. Hence, initial H_2 is released by acid-base reaction between SiO–H and BH_3, leading to surface SiO–B bonds (Figure 6). Further H_2 is formed by dehydropolymerization of the as-formed surface SiO–BH_2–NH_3 and BH_3 of another AB.

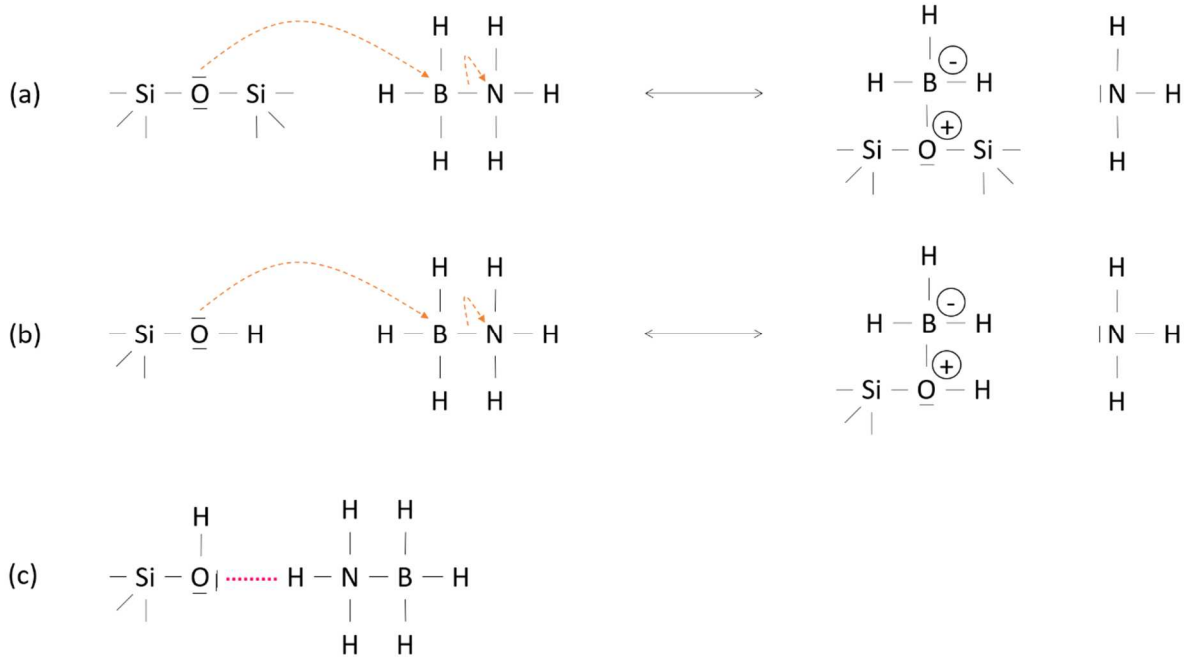

Figure 5. (a, b) Lewis base-acid reaction between O of Si–O–Si or SiO–H (of silica SiO_2) and BH_3 of AB, resulting in the liberation of NH_3. (c) Example of H-bonding interaction between O of SiO–H and NH_3 of AB.

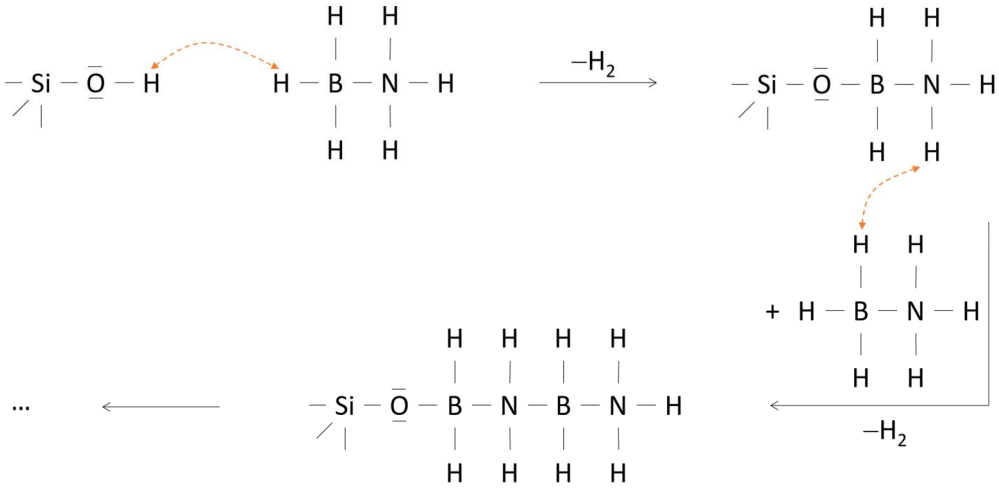

Figure 6. SiO–H group-catalyzed dehydropolymerization of AB.

The third positive effect was evidenced by a series of studies where MCM-41 was used as scaffold [53,54]. Bulk AB and AB@MCM-41 were studied with atomic PDF analysis of synchrotron powder XRD data, anelastic spectroscopy and DSC, over a wide range of temperature (from −193 to 27 °C). The structural evolution of confined AB was compared to

that of bulk AB (Figure 7). Upon warming, bulk AB underwent an order-to-disorder phase transition, from orthorhombic (s.g. *Pmn*2$_1$) to tetragonal (s.g. *I*4*mm*) at –48 °C. In contrast, confined AB was tetragonal in structure between –163 to –33 °C and, a structural change from tetragonal to amorphous occurred between –33 °C and –3 °C. Another study using MCM-41 (as porous nanospheres) also stressed on the amorphous nature of the confined AB at ambient temperature [47]. In amorphous state, AB has altered, i.e. weakened, dihydrogen $H^{\delta+}\cdots H^{\delta-}$ interactions [55], and the AB molecules are more mobile and active [19]. The consequence is modified, greatly improved dehydrogenation properties for AB@scaffold in comparison with bulk AB.

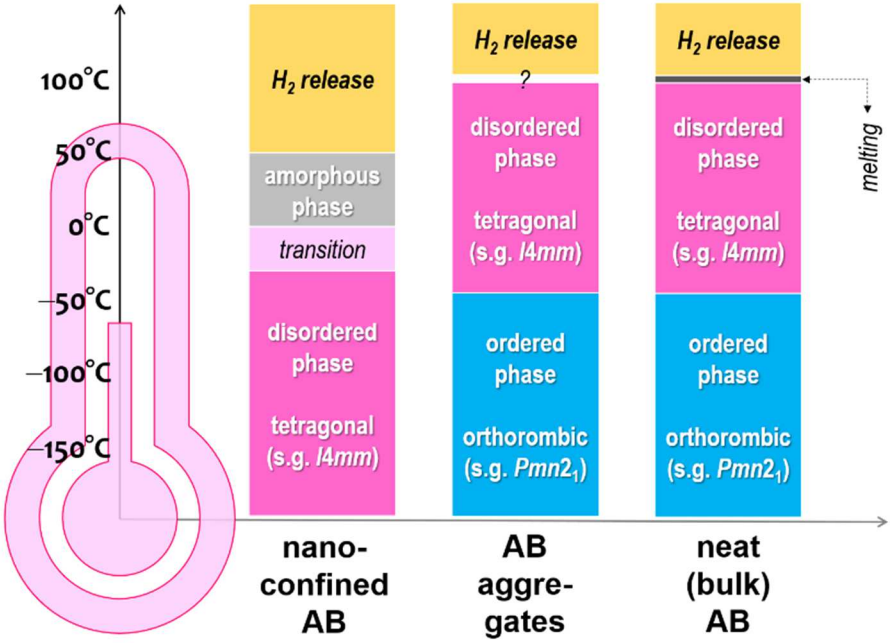

Figure 7. Phase transformation of confined AB, aggregates of AB (i.e. outside the porosity of the scaffold), and bulk AB, from –193 to 150 °C.

2.2. Carbonaceous materials

Feaver et al. [56] proposed carbon as a lighter scaffold than silica and as having better thermal conduction properties. Coherent carbon cryogel (CCC), with a specific surface area of 300 m^2 g^{-1}, a total pore volume of 0.75 cm^3 g^{-1}, and pores of 2-20 nm, was used. Infiltration was done by soaking CCC in a tetrahydrofuran solution of AB. The aggregates of AB deposited on the external surface of the scaffold were washed off. Sepehri et al. [57,58] also used carbon cryogel (CC; 446 m^2 g^{-1} and 1.06 cm^3 g^{-1}) as well as boron- and nitrogen-modified CC (BNCC; 285 m^2 g^{-1} and 0.89 cm^3 g^{-1}), both scaffolds having similar pore size distribution (ca.

16 nm). Infiltration of AB was performed as described above. These studies showed, well before Sullivan et al.'s report [43], that the pore size has a more important role in destabilizing AB than the specific surface area. Controlling the pore size may help in tuning the dehydrogenation temperature of confined AB in such a way that the narrower the pore size is, the lower the peak temperature of H_2 release [59]. In other words, microporosity (pore size of <2 nm) should be favored [60]. For size comparison, it is worth mentioning that the dimensions of the AB molecule are 0.33×0.15 nm^2.

Moussa et al. [61] used activated carbon (AC; 716 m^2 g^{-1} and 0.36 cm^3 g^{-1}) and prepared three different samples, either by infiltrating AB while using a solvent (tetrahydrofuran and methanol) or by ball-milling AB and AC. The best decomposition results were measured for AB@AC using tetrahydrofuran as a solvent. The least attractive destabilization was achieved when methanol was used. This was justified by a less efficient confinement of AB because of a possible repulsion between the surface COO–H groups of AC and the O–H group of methanol. With respect to the ball-milling approach, the as-obtained AB@AC composite showed intermediate performance. Ball-milling could have decreased the size of the AB particles, carbon acting as lubricant during milling, and it could also have favored some confinement of AB. Comparable results were reported by Bravo Diaz et al. [62]. However, the released H_2 was found to be polluted by several by-products including BZ, DB and NH_3. Impregnation of AB in solution was then preferred owing to purer H_2.

In comparison with bulk AB, AB@CCC [56] showed improved dehydrogenation properties, with a one-step release of pure H_2 between 75 and 110 °C. The enthalpy of dehydrogenation was −120 kJ mol^{-1}, which is much more exothermic than that of bulk AB (–21 kJ mol^{-1}). With respect to the AB@CC and AB@BNCC composites [57], comparable decomposition profiles with decreased peak temperatures of dehydrogenation (of 10-15 °C) were observed. However, BZ was still released. The apparent activation energies were lowered, but in a limited extent (150 and 115 kJ mol^{-1} respectively versus 160 kJ mol^{-1} for bulk AB). Li et al. [63] used mesoporous carbon CMK-3 as scaffold (specific surface area of 1150 m^2 g^{-1}, pore volume of 1.29 cm^3 g^{-1}, and pore diameter of 4.5 nm). AB@CMK-3 decomposed into H_2 and NH_3 from about 75 °C and up to 150 °C. The weight loss was as high as 27 wt. % because of the release of NH_3. No BZ was detected. The enthalpy of decomposition was –2.1 kJ mol^{-1}, indicating significantly modified thermodynamics. Comparable results (release of NH_3, no

BZ, enthalpy of −1.6 kJ mol^{-1}, apparent activation energy of 64 kJ mol^{-1}) were reported for AB@AC [61]. Yang et al. [64] used a microporous carbon (MC) with a narrow pore size distribution such as 1-1.5 nm. After infusion of AB by using methanol as a solvent, the specific surface area as well as the pore volume drastically decreased (from 1652 to 56 m^2 g^{-1}, and from 0.87 to 0.04 cm^3 g^{-1}). The resulting AB@MC composite was able to purely dehydrogenate at <50 °C and the dehydrogenation process peaked at 85 °C. The apparent activation energy was 75 kJ mol^{-1}. Similar performance was reported for AB confined into N-containing carbon (i.e. polypyrrole) nanotubes [65].

It is worth mentioning that AB@CCC investigated by Feaver et al. [56] was found to lose some H_2 during the sample preparation. This H_2 formed by reaction of $H^{\delta+}$ from a surface COO–H group and $H^{\delta-}$ of the BH_3 moiety of AB. Such a catalytic activation was also observed with silica as scaffold, but the evolution of H_2 at room conditions had not been reported until AB@CCC. Moussa et al. [61] faced H_2 release at 3-4 °C, which posed safety issues. Because of surface COO–$H^{\delta+}$···$H^{\delta-}$–B interactions, the dihydrogen $H^{\delta+}$···$H^{\delta-}$ network of AB is disrupted and the consequences are a lowered induction period for the dehydrogenation and a lowered barrier to the H_2 formation. Li et al. [63] used XPS to analyze the dehydrogenated form of AB@CMK-3. A binding energy at about 192 eV, typical of B–O bonds, emerged and maintained at high temperatures, indicating the formation of CO–B and COO–B bonds and thus the immobilization of B on the CMK-3 surface (Figure 8). Similar XPS results and conclusions were reported by Cao et al. [66] for AB@CMK-5. Moussa et al. [61] observed the B–O bonds by ^{11}B MAS NMR spectroscopy. Acid catalysis, owing to CO–H and COO–H proton donors, leads to changed dehydrogenation thermodynamics. According to Li et al. [63] and Bravo Diaz et al. [62], acid catalysis cannot hinder – it rather favors – the formation and release of NH_3; in contrast, it hampers the formation and release of BZ. In any case, the acid catalysis effect is believed to overpass the nanosizing effect [67].

Besides the aforementioned acid catalysis effect, the nanosizing effect was reported to also take place. It explains the better dehydrogenation properties of AB confined into the porosity of a carbonaceous scaffold. Nanosizing results in smaller AB crystals with higher surface energy which favors the breaking of B–H and N–H bonds whilst the breaking of the B–N bonds is prevented [64]. In addition, the diffusion path for emitting H_2 is shorter, and the reaction frequency is enhanced, thereby leading to accelerated dehydrogenation [57,63]. A

particularly interesting study showing the positive effect of the nano scale is the one that uses graphene oxide (GO) as host material [68]. By using a tetrahydrofuran solution, 30 and 50 wt. % AB were loaded in the form of nanoparticles and located between the GO sheets to act as spacers. The nanoparticles had a diameter of 4 and 10 nm, respectively. The former ones dehydrogenated starting from 50 °C whereas the latter ones dehydrogenated from 67 °C. The nanoparticles were suggested to form from cationic AB, i.e. $[NH_3BH_2]^+$, as a result of the reaction between $H^{\delta+}$ of surface CO–H and $H^{\delta-}$ of AB, and subsequent $H^{\delta-}$-driven agglomeration of AB molecules around $[NH_3BH_2]^+$. The key role of surface CO–H groups and of their $H^{\delta+}$ in AB dehydrogenation was confirmed by theoretical calculations [69]. In another study using GO [70], the evolution of some NH_3 was noticed for AB@GO. The GO scaffold was partially reduced and was used for AB infiltration. The as-formed composite released, this time, pure H_2. The evolution of NH_3 with AB@GO was attributed to surface CO–H groups.

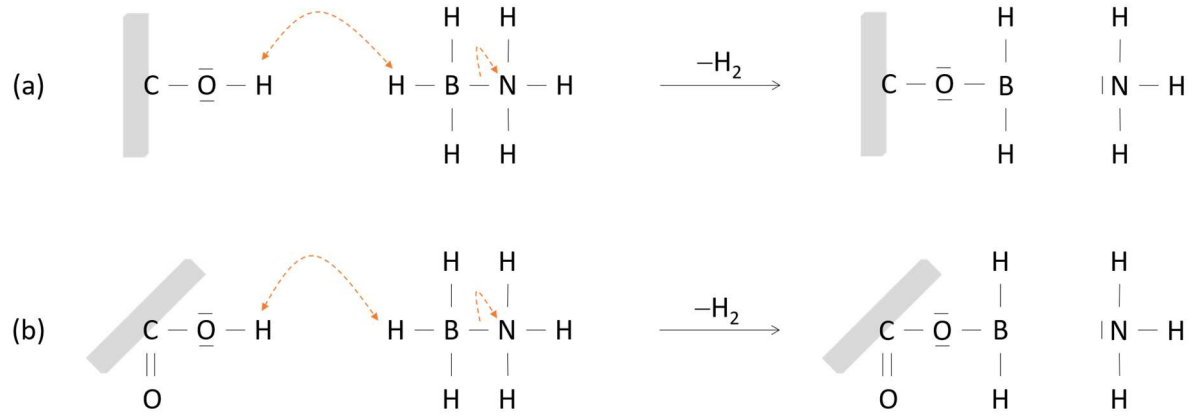

Figure 8. Interactions and reactions between (a) surface CO–H and AB, and (b) surface COO–H and AB, resulting in the formation of surface CO–B and COO–B bonds, the release of H_2 and the generation of NH_3.

The pure confinement effect was demonstrated for a porous aromatic framework (PAF) containing only C and H atoms. Peng et al. [71] focused on PAF-1 which is made of aromatic rings arranged according to the diamond topology and resulting in a light material (0.3 g cm^{-3}) with attractive textural properties (specific surface area of 4657 m^2 g^{-1}, pore volume of 2.55 cm^3 g^{-1}, and pore size of 1.4 nm). AB@PAF-1 dehydrogenated starting from 50 °C, without releasing any gaseous by-product, showing an apparent activation energy of 116 kJ mol^{-1} (184 kJ mol^{-1} for bulk AB in the same experimental conditions).

For AB@CMK-3, Li et al. [63] dug deeper to further improve the dehydrogenation properties in terms of kinetics and purity of the released H_2. The scaffold, prior to the infiltration of AB, was functionalized with 5 wt. % Li^+. The AB@Li^+-CMK-3 composite was then prepared and studied. It showed better dehydrogenation kinetics than the Li^+-free composite (onset temperature of dehydrogenation of 55 °C versus 75 °C) and it released H_2 without NH_3. A synergistic interaction between Li^+ and the surface of CMK-3, featured by CO–Li, was believed to occur, and Li^+ was proposed to play a crucial role in immobilizing the NH_3 group of AB via $Li^+\cdots N$ interactions (Figure 9). Starting from both CO–Li and CO–H as surface groups as well as from one AB, it was suggested the formation of the surface complex $CO–H^{\delta+}\cdots H^{\delta-}–BH_2–H_3N\cdots Li–OC$, as intermediate, for which the B–H and N–H bonds are weakened. Elsewhere, loading Ni^{2+} and Co^{2+} in the form of nanoparticles on the surface of graphene nanosheets were found to improve the dehydrogenation properties of the AB nanophase [72].

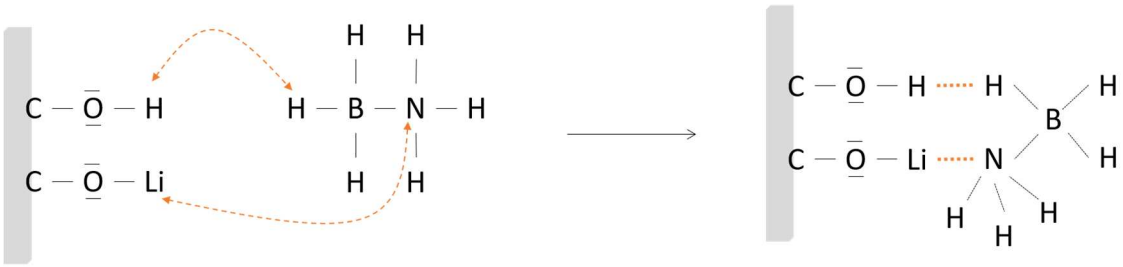

Figure 9. Functionalization of the surface of the carbon CMK-3 by Li^+ and role of Li^+ in the destabilization of AB by immobilization of the NH_3 group via the formation of a doubly anchored AB molecule: $CO–H^{\delta+}\cdots H^{\delta-}–BH_2–H_3N\cdots Li–OC$.

2.3. MOFs

Metal organic frameworks (MOFs) are polymeric materials made of metal cations as coordination sites and organic linkers. They form a wide range of crystalline porous structures and have been considered as potential scaffolds for the AB confinement [73].

The first MOF reported as scaffold is JUC-32-Y [74]. It is made of Y^{3+} sites and 1,3,5-benzentricarloxylate rigid linkers. JUC-32-Y is stable up to 525°C, and by heating below this temperature, water of JUC-32-Y can be removed. Water removal results in the formation of unsaturated Y^{3+} metal sites, expected to strongly interact with AB. A similar process was applied to Mg-MOF-74 (2,5-dioxido-1,4-benzenedicarboxylate linkers), MIL-101 (1,4-benzenedicarboxylate (BDC) linkers), and Zn-MOF-74 (2,5-dihydroxybenzene-1,4-

dicarboxylate linkers) to obtain unsaturated Mg^{2+}, Cr^{3+}, and Zn^{2+} sites respectively [75-77]. Infiltration of AB inside the MOF porosity was done by capillary effect, which was verified by decreased specific surface areas and pore volumes. With a MOF having flexible pores, as is the case for Fe-MIL-53 (Fe^{3+} sites and BDC linkers) [78], the successful confinement of AB was verified by XRD, specifically by determining the unit cell volume before and after infiltration; typically, an increase from 900 to 925 $Å^3$ was noticed after infiltration of AB.

AB@JUC-32-Y dehydrogenated from 50 °C, the dehydrogenation process peaking at 84 °C [74]. AB@Mg-MOF-74 showed an onset temperature of dehydrogenation of <70 °C [75]. With AB@Zn-MOF-74, the temperature was 60 °C [77]. Such positive results were justified by the confinement effect, namely, the considerably increased surface area of nanosized AB and the decreased diffusion path lengths. Besides this, Srinivas et al. [78] stressed on the occurrence of reduced intermolecular interactions between the AB molecules into the porosity of the scaffold. Chung et al. [79] found that there is a linear relationship between the temperature of H_2 desorption and the reciprocal of the AB size (i.e. of the MOF pore size): the narrower the pore size is, the lower the peak temperature of H_2 release. Zhong et al. [80] called this effect into question. By using the chemically and thermally robust ZIF-8 (Zn^{2+} sites and 2-methylimidazolate linkers; 1253 $m^2\ g^{-1}$), they prepared a physical mixture of AB (hand milling using a mortar and a pestle) and ZIF-8, as well as AB@ZIF-8 by infusion using methanol as a solvent. The former showed a specific surface area of 1148 $m^2\ g^{-1}$, and the latter of <66 $m^2\ g^{-1}$. Slightly better dehydrogenation profiles were found with the former sample, allowing the authors to suggest that the confinement may not be the factor promoting AB dehydrogenation. They alternatively suggest a catalytic role of ZIF-8. Contradictory trends were reported for AB@Tm(BTC) (with Tm(BTC) a MOF based on Tm^{3+} sites and 1,3,5-benzenetricarboxylate linkers) prepared by using methanol as AB solvent and another AB@Tm(BTC) elaborated by hand milling [81].

With the AB@MOF composites, an interesting result to discuss is that of the gases released under heating. On the one hand, the released H_2 was found to be pure, especially exempt from NH_3. The absence of NH_3 was attributed to the unsaturated metal sites [82]. These sites act as Lewis acid sites interacting with the electron donor NH_3 moiety of AB and binding to it under heating [83]. Srinivas et al. [78] demonstrated the formation of Fe–NH_2 groups for AB@Fe-MIL-53 upon heating, thereby confirming the role of the metal sites in the AB

dehydrogenation (Figure 10). Partial reduction of Fe^{3+} to Fe^{2+} was observed, but there was no evidence of a complete reduction into Fe^0. With AB@Cu(BDC), the unsaturated Cu^{2+} sites were found to hinder the release of NH_3 also, but Cu^{2+} reduced because of H_2, resulting in partial degradation of the long-range-ordered structure of the MOF (disconnection by broken Cu–O bonds) and weakened confinement effect [84]. On the other hand, some NH_3 was found to be released together with H_2. This was the case for AB@MIL-101 where the Cr^{3+} sites were originally unsaturated [76]. In fact, UV-Vis spectroscopy and XPS results, combined with theoretical calculations, showed that Cr^{3+} was saturated during the preparation of AB@MIL-101, because of the dehydrogenation of AB in some extent, resulting in surface complexes made of NH_2BH_2 and surface CO–Cr (Figure 11). Li et al. [83] investigated AB@MOF-5 (MOF-5 with BDC linkers), knowing that the Zn^{2+} sites were saturated (i.e. fully and tetrahedrally coordinated with carboxylate groups). NH_3 evolved. Similar results were reported for AB@IRMOF-1 (the MOF having Zn^{2+} sites and BDC linkers), AB@IRMOF-10 (the MOF having Zn^{2+} sites and biphenyl-4,4′-dicarboxylate linkers), AB@UiO-66 (the MOF having Zr^{4+} sites and BDC linkers), AB@UiO-67 (the MOF having Zr^{4+} sites and biphenyl-4,4′-dicarboxylate linkers), and AB@MIL-53(Al) (the MOF having Al^{3+} sites and BDC linkers) [79].

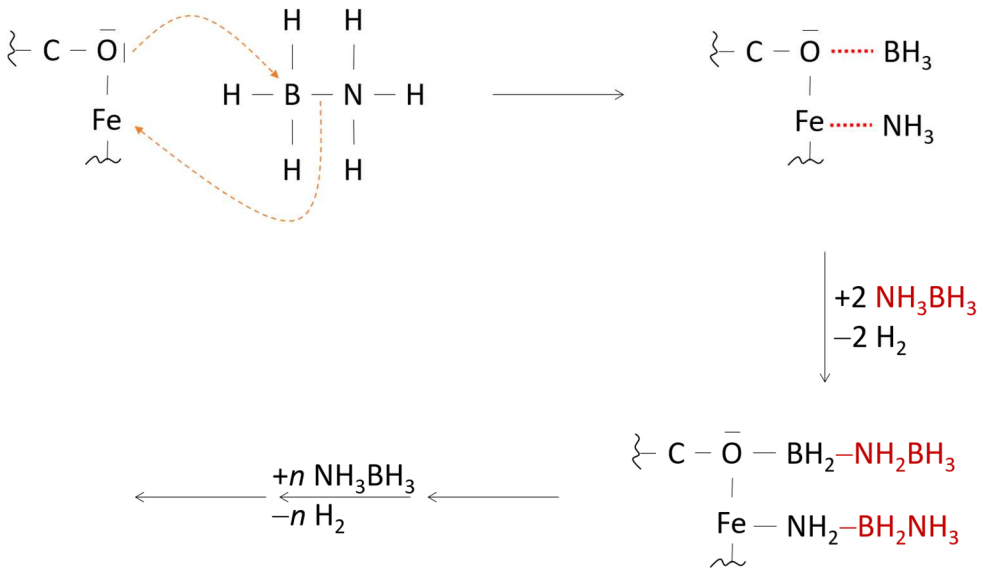

Figure 10. Interaction of AB with the Fe-MIL-53 pore surface, via O···BH_3 and Fe···NH_3, resulting in CO–BH_2 and Fe–NH_2 groups upon reaction with 2 AB molecules.

For dehydrogenated AB@Zn-MOF-74 and AB@Fe-MIL-53 [77,78], FTIR spectroscopy and XPS analyses revealed B–O bonds. These bonds formed by reaction of BH_3 of AB with the

O-functional groups (of the linkers) present inside the pores, suggesting that the destabilization of AB is related to the destabilization of its B–H and B–N bonds. The O-functional groups and the Fe sites have a combined effect for destabilizing AB (Figure 10). Li et al. [83] extrapolated by claiming that the aforementioned O atoms help in avoiding the formation of B_2H_6 by trapping the BH_3 groups. Similar observation was reported by Wu et al. [84] for the MOF Cu(BDC) used as scaffold.

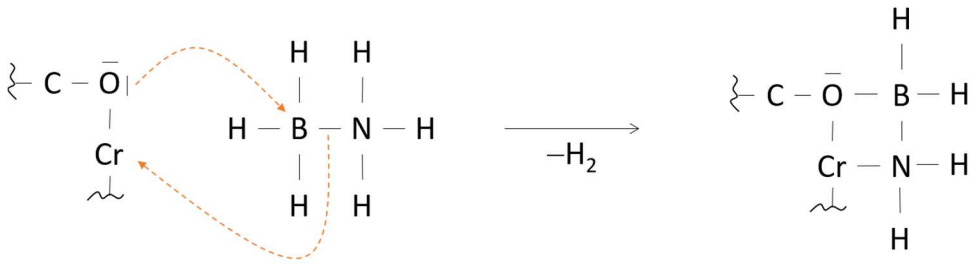

Figure 11. Saturation of the coordination of Cr^{3+} of MIL-101 by reaction with AB during the preparation of AB@MIL-101 and resulting in the formation of NH_2BH_2 bound to the MOF surface via Cr–N and B–O bonds.

Jeong et al. [85] focused on the absence of BZ when AB@MOF-5 was heated. AB@MOF5 released pure H_2, with no detectable volatile by-products. Dehydrogenated AB@MOF5 was analyzed by ^{11}B MAS NMR spectroscopy and no signal suggesting the formation of PB was noticed. They concluded in the formation of polyiminoborane (PIB; structural unit [NHBH]), the linearly linked polymer of AB forming upon the release of 2 equivalents of H_2, which would be favored by the small pores of MOF-5. In other words, the formation of BZ was prevented by the geometric hindrance caused by the small pores. Large surface area and porosity seem to be the key factors to prevent BZ formation.

There is one study for which an unexpected by-product evolved. Si et al. [76] studied AB@MIL-101 which decomposed into aminodiborane $NH_2B_2H_5$ (ADB) together with NH_3. The formation of ADB was explained as follows:

$$2\ NH_3BH_3\ (s) \rightarrow NH_2B_2H_5\ (g) + NH_3\ (g) + H_2\ (g) \quad (3)$$

Furthermore, keeping in mind the surface adsorbed NH_2BH_2 intermediate (Figure 11), ADB could form as follows:

$$NH_3BH_3\ (s) + NH_2BH_2\ (ads) \rightarrow\ NH_2B_2H_5\ (g) + NH_3\ (g) \quad (4)$$

Surface functionalization of MOFs has proven to improve the dehydrogenation properties of confined AB. Si et al. [76] supported Ni on the inner surface of MIL-101 and the resulting AB@Ni/MIL-101, unlike AB@MIL-101, generated pure H_2. The Ni sites hindered the formation of NH_3 and ADB, and they further improved the dehydrogenation kinetics. Gao et al. [86] considered the same MOF but functionalization was done on an ortho carbon of the phenyl group of the organic linker. Functionalization by an amine NH_2 or an amide $NHCOCH_3$ group was done. With (unfunctionalized) AB@MIL-101, the volatile by-products NH_3, DB and BZ formed. After functionalization, some NH_3 was still present. The surface amine groups were suggested to act as chemical immobilizers of AB [87,88].

2.4. Organic polymers

A number of polymers were used (Figure 12). The first polymer reported in the field is poly(methyl acrylate) (PMA) [89]. Dissolved in acetonitrile, it was blended with a solution of AB, resulting in a soft solid that is semi-transparent for 17 wt. % AB and white for 44 wt. % AB. The presence of AB impacted the glass transition temperature of the polymer that decreased from +16.3 °C to –24.5 and –7.4 °C, respectively. The difference was explained by the presence of crystalline AB aggregates. Under heating, AB@PMA showed better decomposition properties than bulk AB. The onset temperature of dehydrogenation was 70 °C for the sample with 17 wt. % AB. Nevertheless, AB@PMA, irrespective to the content of AB, decomposed into H_2 and NH_3. Comparable results were reported for AB@PAM (PAM as polyacrylamide) prepared by blending [90]. For this last study and in ref. [91], water was used as a solvent and interestingly no hydrolysis of AB took place.

With hyper-cross-linked porous polymers (resins) like poly(styrene-co-divinylbenzene) (PSDB), AB dissolved in methanol was loaded by infusion, namely capillary effect. Tang et al. [92] prepared AB@PSDB in this way. The specific surface area and the pore volume of the resin decreased from 757 $m^2\ g^{-1}$ and 0.88 $cm^3\ g^{-1}$ to 215 $m^2\ g^{-1}$ and 0.51 $cm^3\ g^{-1}$. Confined AB was in the form of nanoparticles with a diameter of 4 nm, which was favored by the cross-linked porous structure of PSDB. Pure H_2 was liberated from 50 °C, the reaction enthalpy being –4.7 kJ mol^{-1} and the apparent activation energy 64 kJ mol^{-1}.

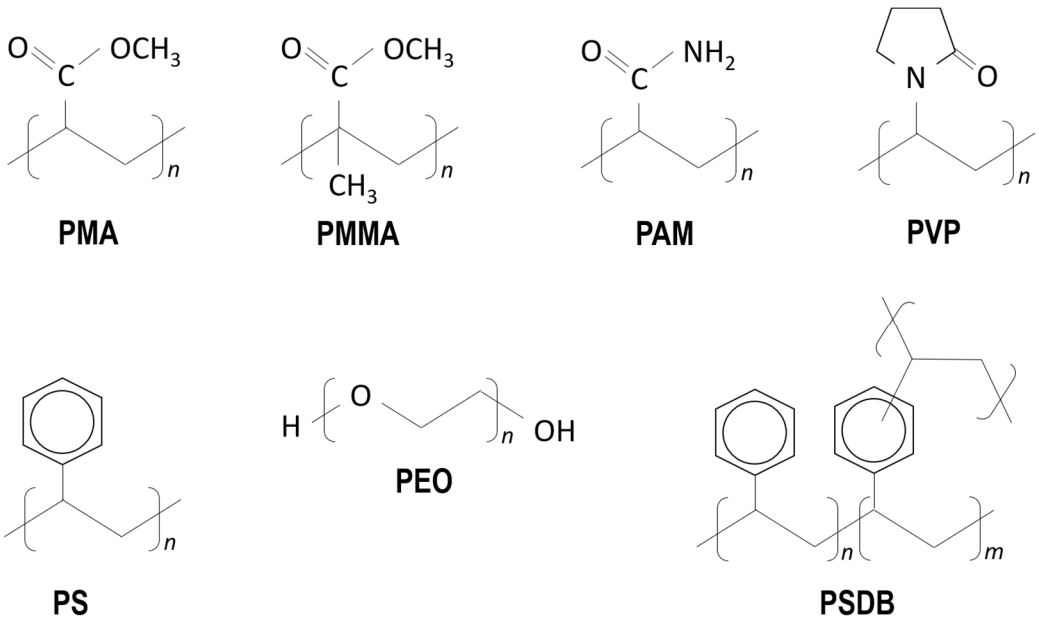

Figure 12. Polymers used as scaffolds for confining AB, with PMA poly(methyl acrylate), PMMA as poly(methyl methacrylate), PAM as polyacrylamide, PVP as polyvinylpyrrolidone, PS as polystyrene, PEO as polyethylene oxide, and PSDB as poly(styrene-co-divinylbenzene).

Another approach for confining AB, precisely in the form of (nano)fibers, is electrospinning where a spinnable polymer plays the role of the scaffold. Kurban et al. [93] reported porous fibers of polystyrene (PS) and AB. The most optimized synthesis produced AB@PS fibers dehydrogenating from 60 °C. Tang et al. [94] electrospun a methanolic solution of polyvinylpyrrolidone (PVP) and AB. AB@PVP fibers with a diameter of 80-100 nm were obtained. They started to dehydrogenate at 60 °C, liberating H_2 contaminated by NH_3. The enthalpy of H_2 release was determined by DSC as being about –4 kJ mol^{-1}. Alipour et al. [95] investigated poly(methyl methacrylate) (PMMA) as polymer for electrospinning AB@PMMA. In comparison to the previous studies, PMMA was not as effective. Formation and release of DB, BZ and NH_3 were observed. By adding a catalyst like carbon nanotubes, pure H_2 formed [96]. With polyethylene oxide (PEO) [97], confined AB released some DB and NH_3, as well as BZ in higher extent than bulk AB. Nevertheless, the dehydrogenation properties of AB@PEO were better than those of bulk AB. This was attributed to the role played by the ethereal O of PEO: the interactions between O and $H^{\delta+}$ of NH_3 of AB replace the dihydrogen $H^{\delta+}\cdots H^{\delta-}$ interactions, resulting in more mobile AB molecules prone to liberate H_2 at low temperatures [98].

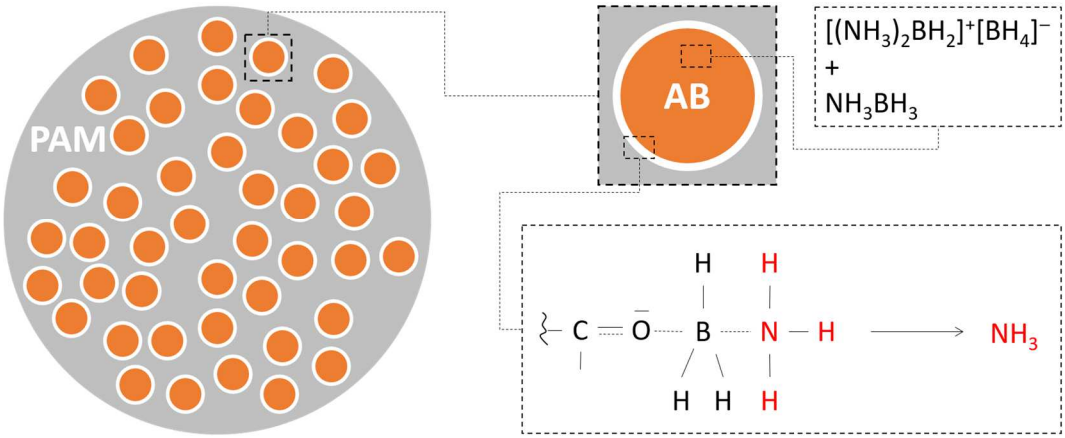

Figure 13. The two decomposition pathways of AB@PAM. The outer shell of the AB nanoparticles decomposes via the formation of surface B–O bonds and rationalizes the evolution of the unwanted NH_3. The core of the AB nanoparticles dehydrogenates according to the DADB initiation pathway, resulting in the formation of linear and cross-linked polymeric residues.

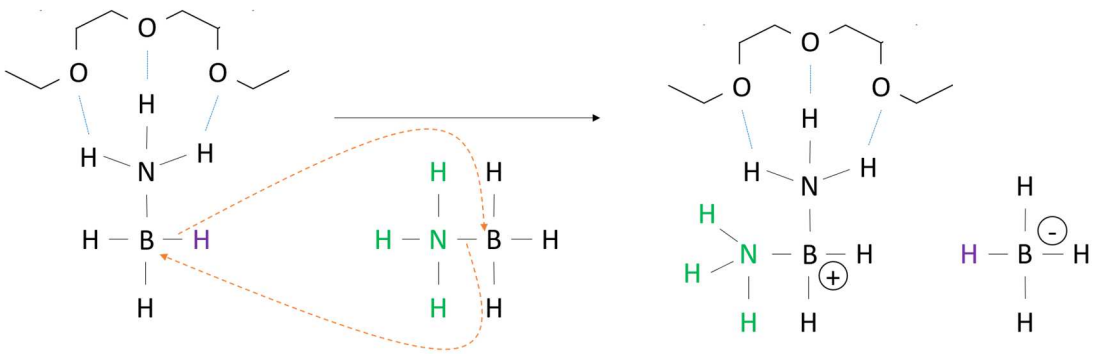

Figure 14. Chemical immobilization of NH_3 of AB via O···H–N hydrogen interactions, and subsequent reaction with another AB molecule resulting in the formation of immobilized DADB.

The improved dehydrogenation properties of AB@PMA, AB@PVP, AB@PMA and AB@PAM can be explained by the formation of C=O···BH_3 bonds and weakened B–H, N–H and B–N bonds. The formation of DB and BZ is hindered due to the formation of B–O bonds, and the B–N bond of AB is weakened resulting in the loss of some NH_3. Li et al. [90] studied AB@PAM by ^{11}B MAS NMR spectroscopy before, during, and after dehydrogenation. The fresh sample showed two BH_3 resonances: the first one was due to the interactions of some BH_3 with the surface C=O groups, and the other one was due to the BH_3 moiety of the AB molecules not interacting with the scaffold surface. Accordingly, the AB nanoparticles were schematized as core@shell systems for which the shell refers to the surface C=O···BH_3 entities and the core to AB (Figure 13). Partially dehydrogenated AB@PAM showed resonances suggesting the presence of AB and DADB, and also the resonance ascribed to the

B–O bond. This supposed the occurrence of the DADB initiation pathway for the core of the AB nanoparticles. Upon complete dehydrogenation, the solid consisted of a mixture of PIB and PB, with a surface made of B–O bonds. Ploszajski et al. [99] also showed the importance of the DADB initiation pathway (Figure 14), in their case for AB@PEO. Upon dehydrogenation (up to 200 °C), AB@PEO led to surface B–O bonds and PB.

2.5. A few other scaffolds

Boron nitride (BN) is the final product of pyrolytic decomposition of AB [100]. It is thermally and chemically stable, and it is made of B and N only, which a priori excludes any risk of contamination of AB because of other elements. It was used for destabilizing AB. For the first studies focusing on BN, a dense material was employed as promoter, not as scaffold. Neiner et al. [101,102] used bulk hexagonal boron nitride (hBN; specific surface area of 12 $m^2\ g^{-1}$) that was mechanically activated to obtain nanocrystallites (ca. 10 nm) developing higher specific surface area (251 $m^2\ g^{-1}$). The hBN nanocrystallites were ball-milled with AB to obtain a mixture denoted AB/hBN. In comparison to bulk AB, AB/hBN showed better decomposition properties. For example, the mixture consisting of 50 wt. % AB and 50 wt. % hBN showed an onset temperature of 90 °C and an enthalpy of 15.1 kJ mol^{-1} (for the first decomposition step). The beneficial effect of hBN was explained by the role it played in disrupting the dihydrogen $H^{\delta+}\cdots H^{\delta-}$ interactions of AB, thereby facilitating the isomerization of AB into DADB. The presence of the hBN nanocrystallites had however a negative impact. AB/hBN generated more BZ than bulk AB did. The BN promoter acted as template and BZ was favorably formed by a surface-enhanced mechanism [103]. Typically, trimers of AB ($[AB]_3$) physically adsorb on the surface of BN through B···N and N···B interactions between the B–N bonds of $[AB]_3$ and those of BN; then the trimers chemically dissociate while liberating H_2 and cyclizing into BZ.

In our group, we focused on porous BN as scaffold [104]. A first example is porous boron nitride nanopolyhedra (BNNP), with a mean diameter of 70 nm (with a wall thickness of 5 nm), a specific surface area of 200.5 $m^2\ g^{-1}$ and a total pore volume of 0.424 $cm^3\ g^{-1}$. Confinement of AB was done by infiltrating a tetrahydrofuran solution of the borane at 0 °C. The as-obtained composite AB@BNNP, with a core@shell structure, showed a specific surface area of 6.7 $m^2\ g^{-1}$ and a total pore volume of 0.023 $cm^3\ g^{-1}$. It was stable below 40 °C. Above this temperature, it dehydrogenated while releasing 1.7 wt. % of pure H_2 up to 80°C.

This was explained by a pure confinement effect. Release of some NH_3 was however observed when the sample was heated above 80 °C. No BZ was detected. A second example is porous hBN in monolithic form (BNM), showing interconnected mesoporous network with a specific surface area of 584 $m^2\ g^{-1}$ and a total pore volume of 0.75 $cm^3\ g^{-1}$ [105]. Unlike for BNNP, pure H_2 was generated thanks to a pure confinement effect.

Yang et al. [106] considered porous manganese oxide MnO_2 hollow cubes (MOHC; 400 nm and a wall thickness of 40 nm) with a specific surface area of 298 $m^2\ g^{-1}$, a porous volume of 1.05 $cm^3\ g^{-1}$, and an average pore diameter of 1.64 nm. AB dissolved in tetrahydrofuran was infiltrated, resulting in decreased specific surface area and pore volume (27.6 $m^2\ g^{-1}$, and 0.27 $cm^3\ g^{-1}$). In comparison with bulk AB, AB@MOHC showed improved dehydrogenation properties such as an onset temperature of 60 °C, the release of pure H_2, and an enthalpy of dehydrogenation of −6 kJ mol^{-1}. More recently, Yang et al. [107] focused once more on porous manganese oxide but in the form of hollow spheres (MOHS). They consisted of porous balls (257 $m^2\ g^{-1}$ and 0.47 $cm^3\ g^{-1}$) of 1-2 µm with a wall thickness of 80 nm. AB@MOHS showed dehydrogenation results that are quite similar to those reported for AB@MCHS. For both scaffolds, the improved dehydrogenation properties were attributed to the nanosizing effect.

3. Comprehensive discussion

3.1. Current understandings

The understanding of the AB confinement strategy as well as of its benefits is rather good. This is discussed hereafter.

Insertion of AB into the porosity of a scaffold is not an issue. There are three approaches that have proven to be effective. The first one uses a solvent of AB like methanol or tetrahydrofuran. The AB solution fills the porosity of the scaffold by capillary effect. It might nonetheless be mentioned that, in tetrahydrofuran, AB would be able to oligomerize/polymerize and the as-formed species could then not effectively diffuse inside the smallest pores. The second approach has been applied to organic polymers, and it also uses solvents. This is the blending method where AB is dissolved in one solvent, the polymer

in the same solvent or in another, and the two solutions are blended. The third approach is solvent free. Typically, the AB and the scaffold are ball-milled. The ball-milling method allows to decrease the size of the AB particles and to partially fill the scaffold porosity with AB. A complete infiltration of AB is unattainable as of yet, at least under the current optimization levels. It is worth repeating that any AB outside the porosity, i.e. AB aggregates, behaves like bulk AB.

Confinement means nanosizing, which is favorable for AB dehydrogenation. This may be conceptualized as follows: the narrower the scaffold pore size is, the smaller the AB nanoparticles, and thus the higher the specific surface area of AB. It follows that, with nanosized AB, the surface energy is higher, there are more defect sites, the intermolecular interactions between the AB molecules are reduced, the AB molecules are more mobile and active, and the diffusion distances are shorter. In other words, the B–H and N–H are weakened, and dehydrogenation is facilitated and accelerated. Concomitantly, the B–N bond is, in some way, reinforced and its breaking prevented. The dehydropolymerization of AB is finally promoted. From the point of the scaffold, microporosity should be favored. Pure confinement effect has been notably shown with BN as a scaffold.

With scaffolds carrying protic hydrogens $H^{\delta+}$ like silica and carbon, AB is destabilized by catalytic activation, namely by interaction of surface $H^{\delta+}$ (from e.g. SiO–H or COO–H) and $H^{\delta-}$ of confined AB. The dihydrogen $H^{\delta+}\cdots H^{\delta-}$ interactions of AB are then disrupted, the induction period for dehydrogenation is considerably shortened, and the barrier to the H_2 formation is lowered. Loss of H_2 was indeed observed during the preparation of the AB@scaffold composite, even at temperatures as low as 3-4 °C. Such catalytic activation outweighs the confinement effect.

The O atoms of scaffolds like silica, carbon, MOF, polymer and manganese oxide also play an important role in destabilizing AB through the formation of $O\cdots BH_3–NH_3$ and/or $O\cdots H–NH_2–BH_3$ interactions. The $O\cdots BH_3–NH_3$ interactions weaken the B–N bond of AB, leading to its breaking and the release of NH_3. Concomitantly, the BH_3 group binds to O, and the as-formed B–O bonds go against the formation of DB and/or BZ. With respect to the $O\cdots H–NH_2–BH_3$ interactions, they replace the dihydrogen $H^{\delta+}\cdots H^{\delta-}$ interactions of the AB molecules. AB is destabilized and liberates H_2 at lower temperatures.

With AB@scaffold, the main volatile by-product is NH_3. The release of NH_3, a Lewis base, can be avoided when unsaturated metal sites acting as Lewis acids are present on the scaffold surface. This may be achieved by supporting a metal cation (e.g. Li^+) onto mesoporous silica or carbon, or by using a thermally activated MOF (e.g. MIL-101 with unsaturated Cr^{3+}). In both cases, the unsaturated metal sites immobilize the NH_3 groups of AB via $Li^+\cdots NH_3$ or $Cr^{3+}\cdots NH_3$ interactions. In contrast, the release of NH_3 cannot be hindered when the metal sites are saturated.

3.2. Limitations and challenges

The confinement strategy has also shortcomings and there are still challenges to be overcome. They are all the more critical because the AB@scaffold composite is intended to be cyclically used.

Scaffolds with surface O–H are problematic. An acid-base reaction between $H^{\delta+}$ and $H^{\delta-}$ of BH_3 of AB may take place, resulting in uncontrolled release of H_2. This precludes any storage of AB@scaffold, even for short time, and for safety reasons. Otherwise, this uncontrolled release of H_2 has two direct consequences. Strong B–O bonds form between the scaffold and the dehydrogenated AB. This is awkward in terms of recyclability (cf. below). Uncontrolled formation of H_2 means wasted H_2, namely, H_2 that is not available for feeding a fuel cell. This results in decreased effective gravimetric hydrogen storage capacities (GHSC). One may wonder whether or not scaffolds carrying surface O–H should be avoided. It is worth mentioning here that a possible alternative could be a N-containing scaffold as predicted by first-principles calculations. Chen et al. [108] predicted that the lone pair of N of the N-containing scaffold would destabilize AB by accepting one of its $H^{\delta+}$, this key initial step being followed by the release of H_2 such as:

$$N^+–H + [NH_2BH_3]^- \rightarrow N + NH_2BH_2 + H_2 \quad (5)$$

MOFs as scaffolds, in comparison with the other ones, have been much studied, and it is quite clear that the best results have been achieved with unsaturated metal sites (e.g. Cr^{3+}, Fe^{3+}, Cu^{2+}). Such sites can be offered for other scaffolds by loading metal cations (e.g. Li^+) into their structure. Yet, two issues have been identified, because of AB. Regarding the first one, AB may coordinate to the electron deficient metal center, saturating it via formation of a

surface complex, and causing the loss of its ability to trap NH_3. The second issue is about the reducing ability of AB [109]. Under heating, AB is able to reduce a metal cation, the reduction being partial (e.g. $Fe^{3+} \rightarrow Fe^{2+}$) or total (e.g. $Cu^{2+} \rightarrow Cu^{0}$). This may deteriorate the MOF effectiveness in driving the release of pure H_2, and even lead to the collapse of the MOF (because of the breaking of metal-oxygen bonds). The chemical stability of MOFs is thus crucial.

By reaction with AB, the formation of B–O bonds has been evidenced for the O-containing scaffolds. For example, B 1s binding energies of ≥191.8 eV were measured by XPS, and these energies are typical of B–O bonds in borate species (e.g. BO_2^-, $B_4O_7^{2-}$, $B(OH)_3$, B_2O_3) [110]. The B–O bond is strong (dissociation energy of 806 kJ mol^{-1}), roughly as strong as the C–O (1076 kJ mol^{-1}) and C=O (749 kJ mol^{-1}) bonds [111]. Transforming B–O bonds into B–H bonds is in fact as challenging as converting C=O bonds (of CO_2) into C–H bonds. It is therefore reasonable to assume that the formation of B–O bonds after dehydrogenation of AB@scaffold is a complicating factor in terms of recyclability and regenerability of AB. To date, no effort has been made regarding this. Future computational and experimental works may shed light on, among others, the dissociation energies of the C–O and B–O bonds of surface C–O–B, the energy barrier to transform the B–O bonds into B–H and N–B bonds, and the conditions allowing the total regeneration of AB. It is also important to know which surface species/complexes may form (C–O–BH_2 and/or C–O–BH_2–NH_3) if the B–O bonds cannot be broken towards the formation of B–H bonds, and how stable they may be. Beyond this, it should be kept in mind that stable B–O bonds mean less B–H bonds after regeneration and thus decreased effective GHSCs.

The aforementioned limitations may act against the cyclic use of AB@scaffold. The limitation regarding the metal sites is particularly acute. Cycle after cycle, extending deconstruction of the MOF scaffold and increasing NH_3 release could be expected. With respect to the limitation due to surface B–O bonds, its impact will be more or less serious: more if the stability and the effective GHSCs of the regenerated AB@scaffold are jeopardized, less if the effective GHSCs are decreased in a negligible or acceptable extent (e.g. <0.5 wt. %). Nevertheless, one thing that should not be overlooked is that the most critical limitation against cyclic use of AB@scaffold is the solid residue forming upon dehydrogenation of confined AB.

Though the exact nature of the solid residues forming upon the dehydrogenation of nanosized AB is not well known, there are three major learnings. B–O bonds form when scaffolds with reactive surface O atoms are used. Upon the release of 1 equivalent of H_2, nanosized AB transforms into various products such as DADB-like intermediates, polyaminoborane (PAB)-, PIB- and PB-like oligomers/polymers; the as-formed solid is thus of complex composition. Upon the release of 2 equivalents of H_2, nanosized AB transforms into PB and/or PIB, but the formation of the latter polymer is favored with scaffolds having pores small enough to prevent dehydrocyclization.

The conclusion emerging from the third point above is that selective formation of pure PB as solid residue seems to be tricky for now. PIB also forms, partially or exclusively. This is a source of concern for the regeneration and cyclic use of AB, since there is no effective chemical route that converts PIB back into AB. When PB forms, the polymer can be re-hydrogenated. For example, Tang et al. [68] attempted to regenerate the solid residue recovered after the dehydrogenation of AB@GO (upon the release of 2 equivalents of H_2) by following the procedure shown in Figure 3. 71% of the starting AB was recovered after a first cycle of regeneration. The percentage decreased to 65% for an extra cycle. To explain these percentages lower than 100%, the authors assumed that some PB was encapsulated and was not accessed by the reducing agent. In our opinion, this might have another prevailing cause, the presence of B–O bonds. As already discussed above, B–O bonds cannot be easily converted into B–H bonds, and it is even thermodynamically impossible in the conditions Tang et al. applied. Another problem not to be overlooked is the risk of draining some PB and/or regenerated AB outside the porosity of the scaffold. Indeed, NH_3 is an excellent solvent of AB and it may promote some AB deconfinement. Against this background, it turns out that it is premature to envision effective dehydrogenation/re-hydrogenation processes over tens/hundreds of cycles. There has been insufficient effort directed toward the cyclability of AB@scaffold.

Another issue is the weight penalty induced by the scaffold. The presence of the scaffold adversely impacts the hydrogen storage capacities of AB. When discussing about GHSCs (as well as volumetric hydrogen storage capacities (VHSCs)), one must be cautious and fair. Prior to any discussion, it is worth well defining what is meant by GHSC. The capacity has to

be seen either from the material level (e.g. AB, AB@scaffold) or from the system level (the system referring to the whole storage system, including tanks, heaters, pipes, valves, electronics, and so forth). At the material level, one has to distinguish between the *theoretical* GHSC, which is the weight percentage of the H atoms in AB or AB@scaffold, and the *effective* GHSC, which is the weight percentage of H_2 that is effectively released as H_2 in operating conditions. At the system level, one has to discuss in terms of *net* GHSC, which is the weight percentage of H_2 effectively released as H_2 on the basis of the weight of the whole storage system. As a first approximation, the *net* GHSC may be seen as half of the *effective* GHSC; this assumes that the weight of AB or AB@scaffold is half of the weight of the storage system.

To illustrate the point above, AB has a *theoretical* GHSC of 19.6 wt. % H. If it is assumed the release of 2.7 equivalents of H_2 (i.e. 90% of AB converted into $[BNH_{0.6}]_n$), the *effective* GHSC is 17.6 wt. % H and the *net* GHSC is 8.8 wt. % H. If it is assumed the formation of $[BNH_2]_n$ (upon the release of 2 equivalents of H_2), the *effective* GHSC is 13.1 wt. % H and the *net* GHSC is 6.55 wt. % H. However, all of these capacities are for bulk AB.

With AB@scaffold, the weight of the scaffold has to be considered. The GHSCs (*theoretical*, *effective*, and *net*) mentioned above have to be revised (Figures 15 and 16) by assuming 10 to 90 wt. % of AB in the composite, and the release of 2.7 equivalents of H_2 (i.e. 90% of AB converted into $[BNH_{0.6}]_n$) or of 2 equivalents of H_2 (i.e. 67% of AB converted into $[BNH_2]_n$). For example, AB@scaffold with 50 wt. % of AB and dehydrogenating at 90% has a *theoretical* GHSC of 9.8 wt. % H, an *effective* GHSC of 8.8 wt. % H and a *net* GHSC of 4.4 wt. % H. Higher loadings (≥60%) should be targeted in order to exceed a *net* GHSC of e.g. 5 wt. % H.

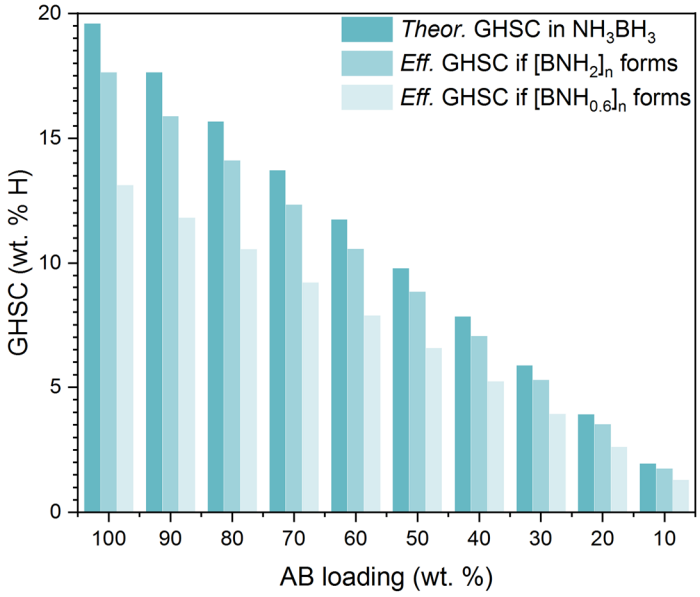

Figure 15. *Effective* (*Eff.*) GHSCs for AB@scaffold with a loading of AB varying from 10 to 90 wt. %. The *theoretical* GHSCs are given. The GHSCs for bulk AB (100 wt. %) are given. The *effective* GHSCs are for dehydrogenation extents of 67% (with formation of $[BNH_2]_n$) and 90% (with formation of $[BNH_{0.6}]_n$).

The solid residues $[BNH_{0.6}]_n$ and $[BNH_2]_n$ represent PB and PIB respectively. The formation of PIB is clearly detrimental in terms of GHSC (Figures 15 and 16). With this polymer, the GHSCs for a conversion of 67% have to be considered which means a *net* GHSC of 3.7 wt. % H. Loadings higher than 80% are then required to exceed a *net* GHSC of 5 wt. % H. It is therefore of importance to identify the dehydrogenated form of AB in order to optimize the dehydropolymerization process and thus the GHSCs.

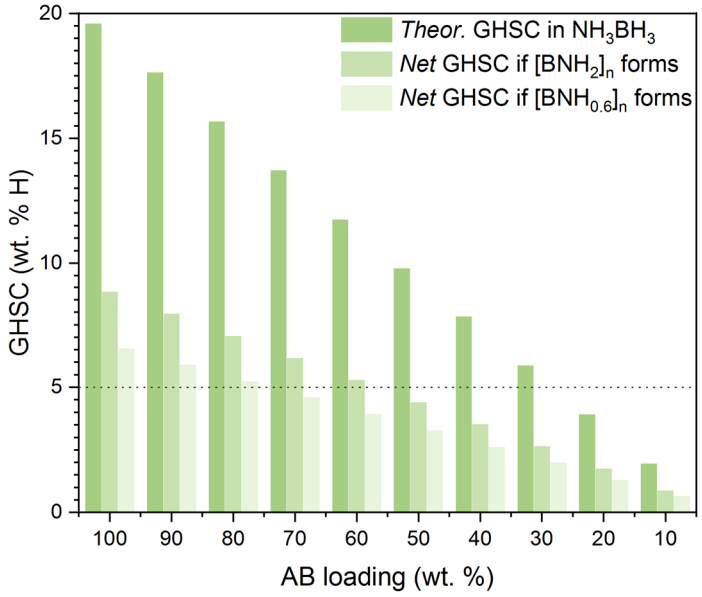

Figure 16. *Net* GHSCs for AB@scaffold with a loading of AB varying from 10 to 90 wt. %. The *theoretical* GHSCs are given. The GHSCs for bulk AB (100 wt. %) are given. The *net* GHSCs are for dehydrogenation extents of 67% (with formation of $[BNH_2]_n$) and 90% (with formation of $[BNH_{0.6}]_n$). The dashed line indicates the GHSC of 5 wt. %.

The *effective* and *net* GHSCs discussed above are valid for a fresh or a fully re-hydrogenated AB@scaffold composite. In the current state, our knowledge of AB cyclability is limited to one report where about 70% of the starting AB was re-hydrogenated. Assuming that 70% of AB is regenerable cycle after cycle, the *net* GHSCs have to be revised downwards (Figure 17). Except for one point, none then reach the level of 5 wt. % H. This is confirmation that AB has to be regenerated while targeting a conversion as close to 100% as possible.

The last but not least challenge is scaling up. Currently, the technological readiness level (TRL) is 3, that is, the concept has been demonstrated experimentally. The next TRL, the 4th one, refers to small scale (or "ugly") prototype built in a laboratory environment. We however have not reached this level yet. It is thus difficult to go further into the discussion without getting into speculation. Only higher TRLs can be proof of the technological relevance and sustainability of the AB confinement strategy. Any prototype should give consolidated *net* GHSCs, and thus a more accurate and more realistic idea of the capacities of the whole storage system.

As a conclusion of the present section, and because the advantages and drawbacks of the scaffolds have been summarized above, a short discussion about the 'good scaffold' candidate might be expected. Comparing the scaffolds reported so far is however tricky because of two main reasons. Firstly, the experimental data (e.g. onset temperature of dehydrogenation, apparent activation energy, enthalpy of dehydrogenation, purity of the released H_2) cannot be relevantly compared because of discrepancies in the experimental conditions (e.g. infiltration procedure, isothermal conditions versus constant heating rate). Secondly, the destabilization of AB by a scaffold carrying surface $H^{\delta+}$ like silica is different, in fact greater, than the destabilization of AB by a MOF that is free of surface $H^{\delta+}$. With the former scaffold, H_2 should be released at a lower temperature than the latter scaffold. However, a new questions raises: is it preferable to release H_2 below 50 °C? Actually, here also, it is difficult to go further into the discussion without getting into speculation. One may however wonder whether silica and carbonaceous materials, for instance the aforementioned SBA-15 and MC, would be the 'good scaffold' candidates based on criteria like abundancy, cost of production, and commercial availability.

3.3. Opportunities

Nanosizing by confinement greatly improves the dehydrogenation properties of AB, but the scaffold causes a weight penalty detrimental in terms of GHSCs. There is thus another avenue to explore. It is to nanosize AB without the use of a scaffold.

Song et al. [112] synthesized, by reaction of DB and NH_3, agglomerated nanoparticles of AB (around 50 nm) together with microsized aggregates of AB. The mixture of these nano- and micro-phases of AB showed slightly better dehydrogenation properties than bulk AB. The sample started to dehydrogenate at 86 °C, and less volatile by-products formed (weight loss of 24.9 wt. % at 200 °C).

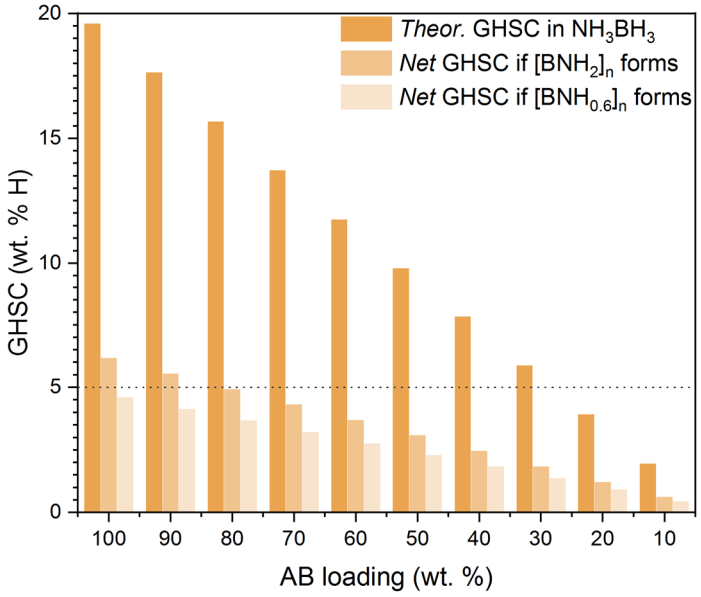

Figure 17. *Net* GHSCs for AB@scaffold with a loading of AB varying from 10 to 90 wt. % and assuming that the residue is re-hydrogenated so that about 70% of the starting AB is recovered. The *theoretical* GHSCs are given. The GHSCs for bulk AB (100 wt. %) are given. The *net* GHSCs are for dehydrogenation extents of 67% (with formation of $[BNH_2]_n$) and 90% (with formation of $[BNH_{0.6}]_n$). The dashed line indicates the GHSC of 5 wt. %.

Recently, we reported nanospheres of AB with an average diameter of 110 nm (Figure 18) [113]. They were obtained by adding dropwise an alkaline aqueous solution of AB and cetyl trimethylammonium bromide $C_{19}H_{39}NH_3Br$ as a surfactant into dodecane $C_{12}H_{26}$ used as antisolvent. Nanosized AB started to dehydrogenate from 80 °C. The improved dehydrogenation properties were attributed to the nanosizing effect. However, above 104 °C, AB melted and the melted samples showed a decomposition pathway that was roughly comparable to that of bulk AB (up to 200 °C). In another attempt [114], nanospheres of AB with an average diameter of 50 nm were synthesized via anti-precipitation method. Tetrahydrofuran was used as a solvent of AB, cyclohexane as antisolvent, and oleic acid $C_{17}H_{33}CO_2H$ as surfactant. However, the AB nanoparticles showed a decomposition profile comparable to that of bulk AB because they melted, and with melting, nanosizing was lost.

To keep the nanosizing effect observed with the scaffold-free nanoparticles of AB, the solution we proposed was to discreetly encapsulate the 50-nm nanospheres of AB with 1-7-nm nanoparticles of metallic Ni [114,115]. The as-obtained composite denoted Ni/AB can be seen as Ni nanoparticles supported on bigger nanoparticles of AB. The approach proved to be

successful since the dehydrogenation started at 50 °C, the melting was suppressed and pure H_2 was released up to 100 °C. These positive results were attributed to the nanosizing effect as well as the catalytic effect of Ni. At higher temperatures, some NH_3 and BZ were however detected. This was explained because the size of the nanoparticles was not small enough.

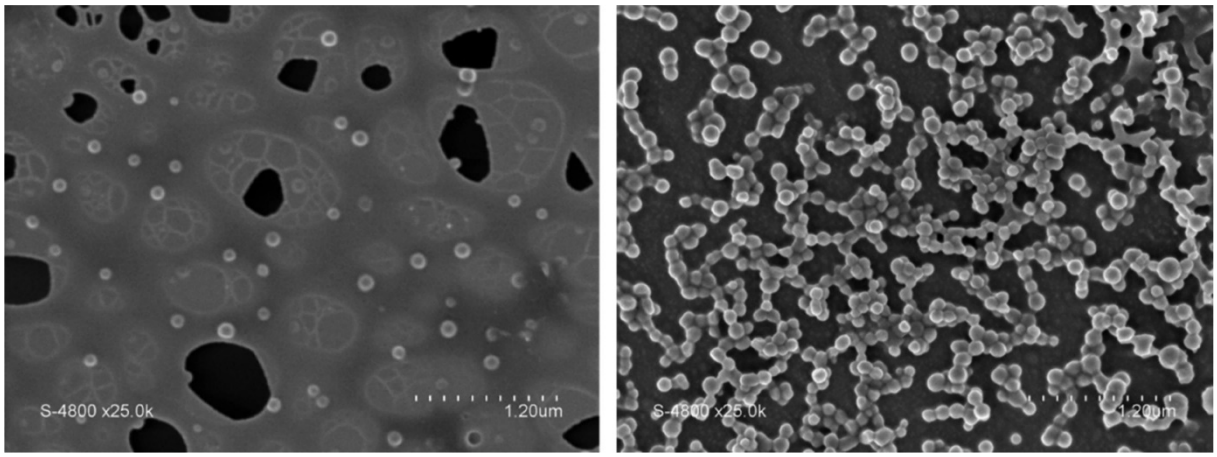

Figure 18. SEM micrographs of AB nanospheres. They were synthesized by adding dropwise 1 mL of AB (0.17 mL min^{-1}) in an aqueous alkaline solution to 1 mL of CTAB in aqueous solution, the as-obtained solution being added dropwise to dodecane (2 mL). The molar ratio AB/CTAB was set at 5060/1. Reprinted with permission from ref. [113]; Copyright (2019) American Chemical Society.

Such achievements open up new opportunities. Further efforts should allow, on the one hand, to further decrease the size of the AB nanoparticles and, on the other hand, to better encapsulate them. Encapsulation can be done by following two strategies. The first one is to optimize the loading and the nature of the catalytic metal nanoparticles. The second one is to elaborate porous metallic shells, made of one metal or bi-/tri-metallic alloys. By optimizing the loading (e.g. <20 wt. %), the GHSCs could be kept high.

4. Conclusion

Discovered in the 1950s, AB was re-discovered in the 2000s to be developed as a solid-state hydrogen storage material and specifically as a solid-state hydrogen storage nano-material. Bulk AB can be nanosized by confinement into the porosity of a scaffold like the seminal mesoporous silica SBA-15. Various scaffolds have been considered to date. Examples are mesoporous silica MCM-41, carbon cryogel, graphene oxide, ZIF-8 and MIL-101 as metal organic frameworks, poly(methyl acrylate) and polystyrene as polymers, boron nitride and

manganese oxide in the form of hollow spheres. In all cases, confined AB shows better dehydrogenation properties than bulk AB. For instance, when the temperatures of dehydrogenation are reduced, H_2 is released in a faster way, much less volatile by-products are formed, and the apparent activation energies are lowered. The better dehydrogenation properties can be explained in terms of a nanosizing effect, but not exclusively. Catalysis effects also contribute in improving the dehydrogenation properties and, in some cases, such an effect overpasses the nanosizing effect. Different catalysis effects take place depending on the nature of the scaffold: namely, a Brønsted acid-base reaction between $H^{\delta+}$ of a surface O–H and $H^{\delta-}$ of AB in the case of silica and carbonaceous scaffolds; a Lewis acid-base reaction between a surface O and B of AB in the case of MOFs and polymer scaffolds; and, Lewis acid-base reaction between an unsaturated metal cation like Cr^{3+} and N of AB in the case of MOFs. The understanding of the destabilization of nanosized AB is thus quite good.

The use of a scaffold has also a number of drawbacks and shortcomings. There are four. (*i*) With a scaffold carrying surface $H^{\delta+}$, Brønsted acid-base reactions take place resulting in uncontrolled H_2 release, related safety issues, and lowered *effective* GHSCs. (*ii*) With a scaffold constituted of surface O, Lewis acid-base reactions lead to the formation of surface B–O bonds that cannot be re-hydrogenated to regenerate B–H bonds and thus AB; this is detrimental in terms of *effective* GHSCs. (*iii*) With a scaffold having unsaturated metal cations, reduction may take place, thereby jeopardizing the beneficial Lewis acid-base reaction between the metal cation and N of AB; another consequence may be the collapse of the scaffold. (*iv*) With any scaffold, there is a weight penalty because of the scaffold weight and the consequence is a decreased *effective* GHSC. These shortcomings are none other than the challenges ahead to still address. As it stands, nanosized AB is not mature enough to envision technological implementation.

For nanosizing AB, to date, preference has been given to hard-templating, i.e. the use of a scaffold. As discussed above, there is room for improvement, especially with regard to lighter, H- and/or O-free scaffolds. Recently, soft-templating has been suggested to be an alternative approach for nanosizing AB. The attractive feature of this approach is that no scaffold is used and accordingly the *effective* GHSCs can be kept high. This is a new sub-field, little studied before. Whether it is hard-templating or soft-templating, there are new

opportunities to explore. Nanosized AB has the potential to be developed further in order to be mature enough for implementation.

References

[1] Abe JO, Popoola API, Ajenifuja E, Popoola OM. Hydrogen energy, economy and storage: Review and recommendation. Int J Hydrogen Energy 2019;44:15072-15086.

[2] Abdin Z, Zafaranloo A, Rafiee A, Mérida W, Lipinski W, Khalilpour KR. Hydrogen as an energy vector. Renew Sust Energy Rev 2020;120:109620.

[3] Dawood F, Anda M, Shafiullah GM. Hydrogen production for energy: An overview. Int J Hydrogen Energy 2020;45:3847-3869.

[4] Moradi R, Groth KM. Hydrogen storage and delivery: Review of the state of the art technologies and risk and reliability analysis. Int J Hydrogen Energy 2019;44:12254-12269.

[5] Andersson J, Grönkvist S. Large-scale storage of hydrogen. Int J Hydrogen Energy 2019;44:11901-11919.

[6] Ren J, Musyoka NM, Langmi HW, Mathe M, Liao S. Current research trends and perspectives on materials-based hydrogen storage solutions: A critical review. Int J Hydrogen Energy 2017;42:289-311.

[7] Boateng E, Chen A. Recent advances in nanomaterial-based solid-state hydrogen storage. Mater Todat Adv 2020;6:100022.

[8] Broom DP, Webb CJ, Fanourgakis GS, Froudakis GE, Trikalitis PN, Hirscher M. Concepts for improving hydrogen storage in nanoporous materials. Int J Hydrogen Energy 2019;44:7768-7779.

[9] Rivard E, Trudeau M, Zaghib K. Hydrogen storage for mobility: A review. Materials 2019;12:1973.

[10] Hirscher M, Yartys VA, Baricco M, von Colbe JB, Blanchard D, Bowman Jr. RC, et al. Materials for hydrogen-based energy storage – past, recent progress and future outlook. J Alloys Compd 2020;827:153548.

[11] Kumar R, Karkamkar A, Bowden M, Autrey T. Solid-state hydrogen rich boron–nitrogen compounds for energy storage. Chem Soc Rev 2019;48:5350-5380.

[12] Schlesinger HI, Burg AB. Recent developments in the chemistry of the boron hydrides. Chem Rev 1942;31:1-41.

[13] Shore SG, Parry RW. The crystalline compound ammoniaborane, H_3NBH_3. J Am Chem Soc 1955;77:6084-6085.

[14] Chandra M, Xu Q. Dissociation and hydrolysis of ammonia-borane with solid acids and carbon dioxide: An efficient hydrogen generation system. J Power Sources 2006;159:855-960.

[15] Akbayrak S, Özkar S. Ammonia borane as hydrogen storage materials. Int J Hydrogen Energy 2018;43:18592-18606.

[16] Dreux KM, McNamara LE, Kelly JT, Wright AM, Hammer NI, Tschumper GS. Probing dative and dihydrogen bonding in ammonia borane with electronic structure computations and Raman under nitrogen spectroscopy. J Phys Chem A 2017;121:5884-5893.

[17] Babenko V, Lane G, Koos AA, Murdock AT, So K, Britton J, et al. Time dependent decomposition of ammonia borane for the controlled production of 2D hexagonal boron nitride. Sci Rep 2017;7:14297.

[18] Kobayashi T, Gupta S, Caporini MA, Pecharsky VK, Pruski M. Mechanism of solid-state thermolysis of ammonia borane: A ^{15}N NMR study using fast magic-angle spinning and dynamic nuclear polarization. J Phys Chem C 2014;118:19548-19555.

[19] Stowe AC, Shaw WJ, Linehan JC, Schmid B, Autrey T. *In situ* solid state ^{11}B MAS-NMR studies of the thermal decomposition of ammonia borane: mechanistic studies of the hydrogen release pathways from a solid state hydrogen storage material. Phys Chem Chem Phys 2007;9:1831-1836.

[20] Wolstenholme DJ, Traboulsee KT, Hua Y, Calhoun LA, McGrady GS. Thermal desorption of hydrogen from ammonia borane: unexpected role of homopolar B–H···H–B interactions. Chem Commun 2012;48:2597-2599.

[21] Al-Kukhun A, Hwang HT, Varma A. Mechanistic studies of ammonia borane dehydrogenation. Int J Hydrogen Energy 2013;38:169-179.

[22] Roy B, Hajari A, Manna J, Sharma P. Supported ammonia borane decomposition through enhanced homopolar B–B coupling. Dalton Trans 2018;47:6570-6579.

[23] Petit JF, Demirci UB. Mechanistic insights into dehydrogenation of partially deuterated ammonia borane NH_3BD_3 being heating to 200 °C. Inorg Chem 2019;58:489-494.

[24] Petit JF, Dib E, Gaveau P, Miele P, Alonso B, Demirci UB. ^{11}B MAS NMR study of the thermolytic dehydrocoupling of two ammonia boranes upon the release of one equivalent of H_2 at isothermal conditions. Chem Select 2017;2:9396-9401.

[25] Sutton AD, Burrell AK, Dixon DA, Garner III EB, Gordon JC, Nakagawa T, et al. Regeneration of ammonia borane spent fuel by direct reaction with hydrazine and liquid ammonia. Science 2011;331:1426-1429.

[26] Rossin A, Peruzzini M. Ammonia-borane and amine-borane dehydrogenation mediated by complex metal hydrides. Chem Soc Rev 2016;116:8848-72.

[27] Denney MC, Pons V, Hebden TJ, Heinekey DM, Goldberg KI. Efficient catalysis of ammonia borane dehydrogenation. J Am Chem Soc 2006;128:12048-12049.

[28] Rossin A, Bottari G, Lozano-Vila AM, Paneque M, Perruzzini M, Rossi A, Zanobini F. Catalytic amine-borane dehydrogenation by a PCP-pincer palladium complex: a combined experimental and DFT analysis of the reaction mechanism. Dalton Trans 2013;42:3533-41.

[29] Kim SK, Han WS, Kim TJ, Nam SW, Mitoraj M, Piekos L, et al. Palladium catalysts for dehydrogenation of ammonia borane with preferential B-H activation. J Am Chem Soc 2010;132:9957-5.

[30] Himmelberger DW, Alden LR, Bluhm ME, Sneddon LG. Ammonia borane hydrogen release in ionic liquids. Inorg Chem 2009; 48:9883-9889.

[31] De Benedetto S, Carewska M, Cento C, Gislon P, Pasquali M, Scaccia S, et al. Effect of milling and doping on decomposition of NH_3BH_3 complex. Thermochim Acta 2006;441:184-190.

[32] Heldebrant DJ, Karkamkar A, Hess NJ, Bowden M, Rassat S, Zheng F, et al. The effects of chemical additives on the induction phase in solid-state thermal decomposition of ammonia borane. Chem Mater 2008;20:5332-5336.

[33] Gutowska A, Li L, Shin Y, Wang CM, Li XS, Linehan JC, et al. Nanoscaffold mediates hydrogen release and the reactivity of ammonia borane. Angew Chem 2005;44:3578-3582.

[34] Chua YS, Chen P, Wu G, Xiong Z. Development of amidoboranes for hydrogen storage. Chem Commun 2011;47:5116-5129.

[35] de Jongh PE, Adelhelm P. Nanosizing and nanoconfinement: New strategies towards meeting hydrogen storage goals. ChemSusChem 2010;3:1332-48.

[36] Nielsen TK, Besenbacher F, Jensen TR. Nanoconfined hydrides for energy storage. Nanoscale 2011;3:2086-98.

[37] Yu X, Tang Z, Sun D, Ouyang L, Zhu M. Recent advances and remaining challenges of nanostructured materials for hydrogen storage applications. Progr Mater Sci 2017;88:1-48.

[38] Rueda M, Sanz-Moral LM, Martin A. Innovative methods to enhance the properties of solid hydrogen storage materials based on hydrides through nanoconfinement: A review. J Supercrit Fluids 2018;141:198-217.

[39] Wahab MA, Zhao Y, Yao XD. Nano-confined ammonia borane for chemical hydrogen storage. Front Chem Sci Eng 212;6:27-33.

[40] Petit JF, Miele P, Demirci UB. Ammonia borane H_3N-BH_3 for solid-state chemical hydrogen storage: different samples with different thermal behaviors. Int J Hydrogen Energy 2016;41:15462-15470.

[41] Petit JF, Demirci UB. Discrepancy in the thermal decomposition/dehydrogenation of ammonia borane screened by thermogravimetric analysis. Int J Hydrogen Energy 2019;44:14201-14206.

[42] Zhang T, Yang X, Yang S, Li D, Cheng F, Tao Z, et al. Silica hollow nanospheres as new nanoscaffold materials to enhance hydrogen releasing from ammonia borane. Phys Chem Chem Phys 2011;13:18592-18599.

[43] Sullivan JA, Herron R, Phillips AD. Towards an understanding of the beneficial effect of mesoporous materials on the dehydrogenation characteristics of NH_3BH_3. Appl Catal B Env 2017;201:182-188.

[44] Wang LQ, Karkamkar A, Autrey T, Exarhos GJ. Hyperpolarized ^{129}Xe NMR investigation of ammonia borane in mesoporous silica. J Phys Chem C 2009;113:6485-6590.

[45] Lai SW, Lin HL, Yu TL, Lee LP, Weng BJ. Hydrogen release from ammonia borane embedded in mesoporous silica scaffolds: SBA-15 and MCM-41. Int J Hydrogen Energy 2012;37:14393-14404.

[46] Rueda M, Sanz-Moral LM, Segovia JJ, Martín A. Improvement of the kinetics of hydrogen release from ammonia borane confined in silica aerogel. Microp Mesop Mater 2017;237:189-200.

[47] Zhao Y, Zhang J, Akins DL, Lee JW. Effect of composition on dehydrogenation of mesoporous silica/ammonia borane nanocomposites. Ind Eng Chem Res 2011;50:10024-10028.

[48] Valero-Pedraza MJ, Gascon V, Carreon M, Leardini F, Ares JR, Martín A, et al. *Operando* Raman-mass spectrometry investigation of hydrogen release by thermolysis of ammonia borane confined in mesoporous materials. Microp Mesop Mater 2016;226:454-465.

[49] Roy B, Manna J, Pal U, Hajari A, Bishnoi A, Sharma P. An in situ study on the solid state decomposition of ammonia borane: unmitigated by-product suppression by a naturally abundant layered clay mineral. Inorg Chem Front 2018;5:301-309.

[50] Xin G, Yang J, Li W, Zheng J, Li X. Catalytic thermal decomposition of ammonia–borane by well-dispersed metal nanoparticles on mesoporous substrates prepared by magnetron sputtering. Eur J Inorg Chem 2012;2012:5722-5728.

[51] Rueda M, Sanz-Moral LM, Nieto-Márquez A, Longone P, Mattea F, Martín A. Production of silica aerogel microparticles loaded with ammoniaborane by batch and semicontinuous supercritical drying techniques. J Supercrit Fluids 2014;92:299-310.

[52] Feng Y, Zhou X, Yang JH, Gao X, Yin L, Zhao Y, et al. Encapsulation of ammonia borane in Pd/halloysite nanotubes for efficient thermal dehydrogenation. ACS Sust Chem Eng 2010;8:2122-2129.

[53] Kim H, Karkamkar A, Autrey T, Chupas P, Proffen T. Determination of structure and phase transition of light element nanocomposites in mesoporous silica: Case study of NH_3BH_3 in MCM-41. J Am Chem Soc 2009;131:13749-13755.

[54] Paolone A, Palumbo O, Rispoli P, Cantelli R, Autrey T, Karkamkar A. Absence of the structural phase transition in ammonia borane dispersed in mesoporous silica: evidence of novel thermodynamic properties. J Phys Chem C 2009;113:10319-10321.

[55] Richard J, Cid SL, Rouquette J, van de Lee A, Bernard S, Haines J. Pressure-induced insertion of ammonia borane in the siliceous zeolite, silicalite-1F. J Phys Chem C 2016;120:9334-9340.

[56] Feaver A, Sepehri S, Shamberger P, Stowe A, Autrey T, Cao G. Coherent carbon cryogel-ammonia borane nanocomposites for H_2 storage. J Phys Chem B 2007;111:7469-7472.

[57] Sepehri S, Garcia BB, Cao G. Influence of surface chemistry on dehydrogenation in carbon cryogel ammonia borane nanocomposites. Eur J Inorg Chem 2009;2009:599-603.

[58] Sepehri S, Garcia BB, Cao G. Influences of surface chemistry on dehydrogenation of ammonia borane in porous carbon scaffold. Adv Mater Res 2010;132: 19-28.

[59] So SH, Jang JH, Sung SJ, Yang SJ, Nam KT, Park CR. Demonstration of the nanosize effect of carbon nanomaterials on the dehydrogenation temperature of ammonia borane. Nanoscale Adv 2019;1:4697-4703.

[60] Klooster WT, Koetzle TF, Siegbahn PEM, Richardson TB, Crabtree RH. Study of the N–H···H–B dihydrogen bond including the crystal structure of BH_3NH_3 by neutron diffraction. J Am Chem Soc 1999;121:6337-6343.

[61] Moussa G, Bernard S, Demirci UB, Chiriac R, Miele P. Room-temperature hydrogen release from activated carbon-confined ammonia borane. Int J Hydrogen Energy 2012;37:13437-13445.

[62] Bravo Diaz L, Hanlon JM, Bielewski M, Milewska A, Gregory DH. Ammonia borane based nanocomposites as solid-state hydrogen stores for portable power applications. Energy Technol 2018;6:583-594.

[63] Li L, Yao X, Sun C, Du A, Cheng L, Zhu Z, et al. Lithium-catalyzed dehydrogenation of ammonia borane within mesoporous carbon framework for chemical hydrogen storage. Adv Funct Mater 2009;19:265-271.

[64] Yang Z, Zhou D, Chen B, Liu Z, Xia Q, Zhu Y, et al. Improved hydrogen release from ammonia borane confined in microporous carbon with narrow pore size distribution. J Mater Chem A 2017;5:15395-15400.

[65] Zhang L, Xia G, Ge Y, Wang C, Guo Z, Li X, Yu X. Ammonia borane confined by nitrogen-containspeing carbon nanotubes: enhanced dehydrogenation properties originating from synergetic catalysis and nanoconfinement. J Mater Chem A 2015;3: 20494-20499.

[66] Cao Z, Ouyang L, Felderhoff M, Zhu M. Low temperature dehydrogenation properties of ammonia borane within carbon nanotube arrays: a synergistic effect of nanoconfinement and alane. RSC Adv 2020;10:19027-19033.

[67] Sepehri S, Feaver A, Shaw WJ, Howard CJ, Zhang Q, Autrey T, et al. Spectroscopic studies of dehydrogenation of ammonia borane in carbon cryogel. J Phys Chem C 2007;111:14285-14289.

[68] Tang Z, Chen H, Chen X, Wu L, Yu X. Graphene oxide based recyclable dehydrogenation of ammonia borane within a hybrid nanostructure. J Am Chem Soc 2012;134:5464-5467.

[69] Kuang A, Liu T, Kuang M, Yang R, Huang R, Wang G, et al. Hydrogen bonding-mediated dehydrogenation in the ammonia borane combined graphene oxide systems. Physica E 2018;97:75-81.

[70] Champet S, van den Berg J, Szczesny R, Godula-Jopek A, Gregory DH. Nano-inclusion in one step: spontaneous ice-templating of porous hierarchical nanocomposites for selective hydrogen release. Sust Energy Fuels 2019;3:396-400.

[71] Peng Y, Ben T, Jia Y, Yang D, Zhao H, Qiu S, et al. Dehydrogenation of ammonia borane confined by low-density porous aromatic framework. J Phys Chem C 2012;116:25694-25700.

[72] Sun W, Li H, Wang Y. Graphene-supported nickel chloride and cobalt chloride nanoparticles as highly efficient catalysts for dehydrogenation of ammonia borane. Int J Hydrogen Energy 2015;40:15389-15397.

[73] Rossin A, Tuci G, Luconi L, Giambastiani G. Metal–organic frameworks as heterogeneous catalysts in hydrogen production from lightweight inorganic hydrides. ACS Catal 2017;7:5035-45.

[74] Li Z, Zhu G, Lu G, Qiu S, Yao X. Ammonia borane confined by a metal-organic framework for chemical hydrogen storage: Enhancing kinetics and eliminating ammonia. J Am Chem Soc 2010;132:1490-1491.

[75] Gadipelli S, Ford J, Zhou W, Wu H, Udovic TJ, Yildirim T. Nanoconfinement and catalytic dehydrogenation of ammonia borane by magnesium-metal-organic-framework-74. Chem Eur J 2011;17:6043-6047.

[76] Si XL, Sun LX, Xu F, Jiao CL, Li F, Liu SS, et al. Improved hydrogen desorption properties of ammonia borane by Ni-modified metal-organic frameworks. Int J Hydrogen Energy 2011;36:6698-6704.

[77] Srinivas G, Ford J, Zhou W, Yildirim T. Zn-MOF assisted dehydrogenation of ammonia borane: Enhanced kinetics and clean hydrogen generation. Int J Hydrogen Energy 2012;37:3633-3638.

[78] Srinivas G, Travis W, Ford J, Wu H, Guo ZX, Yildirim T. Nanoconfined ammonia borane in a flexible metal-organic framework Fe–MIL-53: clean hydrogen release with fast kinetics. J Mater Chem A 2013;1:4167-4172.

[79] Chung JY, Liao CW, Chang YW, Chang BK, Wang H, Li J, et al. Influence of metal-organic framework porosity on hydrogen generation from nanoconfined ammonia borane. J Phys Chem C 2017;121:27369-27378.

[80] Zhong RQ, Zou RQ, Nakagawa T, Janicke M, Semelsberger TA, Burrell AK, et al. Improved hydrogen release from ammonia-borane with ZIF-8. Inorg Chem 2012;51:2728-2730.

[81] Yang H, Li Z, Liu K, Meng F, Niu C. Clean hydrogen release from ammonia borane in a metal-organic framework with unsaturated coordinated Tm^{3+}. J Phys Chem C 2015;119:2260-2265.

[82] Kong S, Dai R, Li H, Sun W, Wang Y. Microwave hydrothermal synthesis of Ni-based metal-organic frameworks and their derived yolk-shell NiO for Li-ion storage and supported ammonia borane for hydrogen desorption. ACS Sust Chem Eng 2015;3:1830-1838.

[83] Li Z, Liu W, Yang H, Sun T, Liu K, Wang Z, Niu C. Improved thermal dehydrogenation of ammonia borane by MOF-5. RSC Adv 2015;5:10746-10750.

[84] Wu YJ, Wang CY. Insight into the catalytic effects of open metal sites in metal-organic frameworks on hydride dehydrogenation via nanoconfinement. ACS Sust Chem Eng 2019;7:16013-16025.

[85] Jeong HM, Shin WH, Park JH, Choi JH, Kang JK. A metal–organic framework as a chemical guide to control hydrogen desorption pathways of ammonia borane. Nanoscale 2014;6:6526-6530.

[86] Gao L, Li CYV, Yung H, Chan KY. A functionalized MIL-101(Cr) metal–organic framework for enhanced hydrogen release from ammonia borane at low temperature. Chem Commun 2013;49:10629-10631.

[87] Wang X, Xie L, Huang KW, Lai Z. A rationally designed amino-borane complex in a metal organic framework: a novel reusable hydrogen storage and size-selective reduction material. Chem Commun 2015;51:7610-7613.

[88] Liao CW, Tseng PS, Chang BK, Wang CY. Facilitated hydrogen release kinetics from amine borane functionalization on gate-opening metal-organic framework. Surf Coat Technol 2018;350:12-19.

[89] Zhao J, Shi J, Zhang X, Cheng F, Liang J, et al. A soft hydrogen storage material: poly(methyl acrylate)-confined ammonia borane with controllable dehydrogenation. Adv Mater 2009;22:394-397.

[90] Li SF, Tang ZW, Tan YB, Yu XB. Polyacrylamide blending with ammonia borane: A polymer supported hydrogen storage composite. J Phys Chem C 2012;116:1544-1549.

[91] Seemaladinne R, Pati S, Kharel K, Bafana A, al-Wahish A, Wujcik EK, et al. Ammonia borane with polyvinylpyrrolidone as a hydrogen storage material: Comparison of different molecular weights. J Phys Chemistry Solids 2017;110:394-400.

[92] Tang Z, Li S, Yang W, Yu X. Hypercrosslinked porous poly(styrene-co-divinylbenzene) resin: a promising nanostructure-incubator for hydrogen storage. J Mater Chem 2012;22:12752-12758.

[93] Kurban Z, Lovell A, Bennington SM, Jenkins DWK, Ryan KR, Jones MO, etc. A solution selection model for coaxial electrospinning and its application to nanostructured hydrogen storage materials. J Phys Chem C 2010;114:21201-21213.

[94] Tang Z, Li S, Yang Z, Yu X. Ammonia borane nanofibers supported by poly(vinyl pyrrolidone) for dehydrogenation. J. Mater Chem 2011;21:14616-14621.

[95] Alipour J, Shoushtari AM, Kaflou A. Electrospun PMMA/AB nanofiber composites for hydrogen storage applications. e-Polymers 2014;14:305-311.

[96] Alipour J, Shoushtari AM, Kaflou A. Ammonia borane confined by poly(methyl methacrylate)/multiwall carbon nanotube nanofiber composite, as a polymeric hydrogen storage material. J Mater Sci 2015;50:3110-3117.

[97] Nathanson AS, Ploszajski AR, Billing M, Cook JP, Jenkins DWK, Headen TF, et al. Ammonia borane–polyethylene oxide composite materials for solid hydrogen storage. J Mater Chem A 2015;3:3683-3691.

[98] Ploszajski AR, Billing M, Cockcroft JK, Skipper NT. Crystalline structure of an ammonia borane-polyethylene oxide cocrystal: a material investigated for its hydrogen storage potential. Cryst Eng Comm 2018;20;4436-4440.

[99] Ploszajski AR, Billing M, Nathanson AS, Vickers S, Bennington SM. Freeze-dried ammonia borane-polyethylene oxide composites: Phase behaviour and hydrogen release. Int J Hydrogen Energy 2018;43:5645-5656.

[100] Frueh S, Kellett R, Mallery C, Molter T, Willis WS, King'ondu C, et al. Pyrolytic decomposition of ammonia borane to boron nitride. Inorg Chem 2011;50:783-792.

[101] Neiner D, Karkamkar A, Linehan JC, Arey B, Autrey T, Kauzlarich SM. Promotion of hydrogen release from ammonia borane with mechanically activated hexagonal boron nitride. J Phys Chem C 2009;113:1098-1103.

[102] Neiner D, Luedtke A, Karkamkar A, Shaw W, Wang J, Browning ND, et al. Decomposition pathway of ammonia borane on the surface of nano-BN. J Phys Chem C 2010;114:13935-13941.

[103] Peyghan AA, Aslanzadeh SA, Samiei A. Ammonia borane reaction with a BN nanotube: a hydrogen storage route. Monatsh Chem 2014;145:1083-1087.

[104] Moussa G, Demirci UB, Malo S, Bernard S, Miele P. Hollow core@mesoporous shell boron nitride nanopolyhedron-confined ammonia borane: a pure B–N–H composite for chemical hydrogen storage. J Mater Chem A 2014;2:7717-7722.

[105] Salameh C, Moussa G, Bruma A, Fantozzi G, Malo S, Miele P, et al. Robust 3D boron nitride nanoscaffolds for remarkable hydrogen storage capacity from ammonia borane. Energy Technol 2018;6:570-577.

[106] Yang Z, Liang J, Cheng F, Tao Z, Chen J. Porous MnO2 hollow cubes as new nanoscaffold materials for the dehydrogenation promotion of ammonia-borane (AB). Microp Mesop Mater 2012;161:40-47.

[107] Yang Z, Sun H, Li H, Li F, Qijing H, Zhang Y. Enhancing the thermal dehydrogenation properties of ammonia borane (AB) by using monodisperse MnO_2 hollow spheres (MHS). J Alloys Compd 2019;781:111-117.

[108] Chen X, Wan L, Huang J, Ouyang L, Zhu M, Guo Z, Yu X. Nitrogen-containing carbon nanostructures: A promising carrier for catalysis of ammonia borane dehydrogenation. Carbon 2014;68:462-72.

[109] Kalidindi SB, Sanyal U, Jagirdar BR. Chemical synthesis of metal nanoparticles using amine-boranes. Chem Sus Chem 2011;4:317-324.

[110] NIST X-ray Photoelectron Spectroscopy Database, https://srdata.nist.gov/xps/; 2012.

[111] Haynes WM. CRC Handbook of Chemistry and Physics. 97th ed. Boca Raton: CRC Press Taylor & Francis Group; 2017.

[112] Song Y, Ma N, Ma X, Fang F, Chen X, Guo Y. Synthesis of ammonia borane nanoparticles and the diammoniate of diborane by direct combination of diborane and ammonia. Chem Eur J 2016;22:6228-6233.

[113] Valero-Pedraza MJ, Cot D, Petit E, Aguey-Zinsou FK, Alauzun JG, Demirci UB. Ammonia borane nanospheres for hydrogen storage. ACS Appl Nano Mater 2019;2:1129-1138.

[114] Lai Q, Rawal A, Quadir MZ, Cazorla C, Demirci UB, Aguey-Zinsou FK. Nanosizing ammonia borane with nickel: A path toward the direct hydrogen release and uptake of B-N-H systems. Adv Sust Syst 2017;2:1700122.

[115] Lai Q, Aguey-Zinsou FK, Demirci UB. Nanosizing ammonia borane with nickel – An all-solid and all-in-one approach for H_2 generation by hydrolysis. Int J Hydrogen Energy 2018;43:14498-14506.

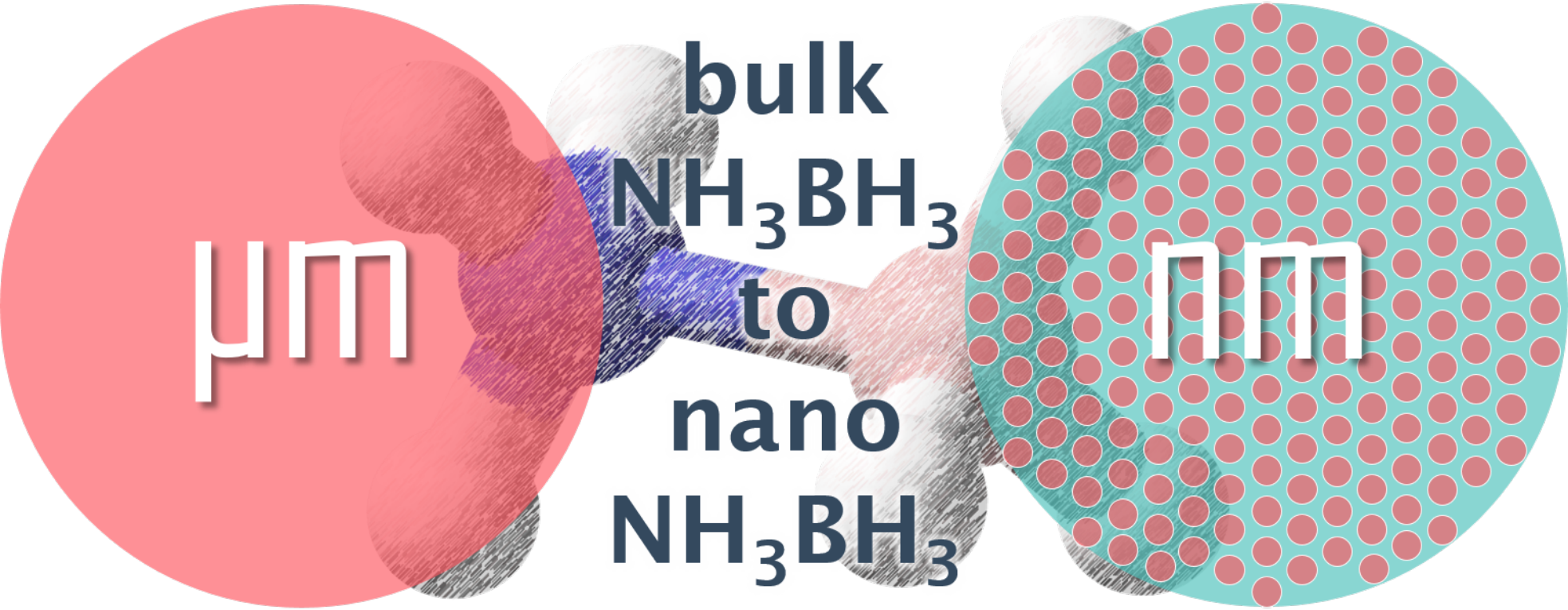
μm
bulk
NH_3BH_3
to
nano
NH_3BH_3
nm